Cretaceous intermediate sulfidation ore system in the Dongkeng Volcanic Basin, SE China: constraints from the Dongji and Maluntou gold deposits

Meng–Ting Chen[a*], Jun–Hao Wei[b], David Selby[b,c],

Yan–Jun Li[b], Wen–Jie Shi[b], Yu–Jing Zhao[d]

[a] *School of Geology and Mining Engineering, Xinjiang University, Urumqi 830000, China*

[b] *School of Earth Resources, China University of Geosciences, Wuhan 430074, China*

[c] *Department of Earth Sciences, Durham University, Durham DH1 3LE, United Kingdom*

[d] *Xinjiang Geological Survey Institute, Urumqi 830000, China*

Corresponding author

Meng–Ting Chen

School of Geology and Mining Engineering, Xinjiang University

No. 1230 Yanan Road, Tianshan District, Urumqi, Xinjiang, 830000, P.R. China

mail: cmt@cug.edu.cn

Abstract

The Dongji (>12.5 t Au @ 4.27 g/t) and Maluntou (>5.0 t Au @ 3.70 g/t) gold deposits are the two largest ones in the Dongkeng Volcanic Basin (DVB), SE China, that are hosted by volcanic rocks. Mineralization is represented by three stages (i.e., stage 1, 2, and 3) that are characterized by four types of unzoned hydrothermal pyrite (i.e., pyrite1, 2a, 2b, and 3). Hydrothermal fluids responsible for pyrite1 deposition are moderate temperatures (308−377 °C) and low salinity (4.6−9.1 wt% NaCl equiv.). The deposition of pyrite2a and 2b is related to the stage 2 fluids featured by moderate-low temperatures (253−341 °C) and low salinity (3.2−9.1 wt% NaCl equiv.). Pyire3 is deposited from the stage 3 fluids with low temperatures (220−250 °C) and salinities (1.0−6.5 wt% NaCl equiv.). Hydrothermal fluids potentially have a magmatic origin and experience fluid boiling and mixing of meteoric water.

Scanning electron microscopy and laser ablation inductively coupled plasma-mass spectrometry were used to investigate the occurrence of visible gold and the distribution of invisible gold in pyrite from different generations. Visible gold mainly exists as native gold and electrum within crystal interstices, fractures, and hollows of pyrite2b, and precipitates directly from the fluids during fluid boiling at ca. 329 °C with pressure of ca.120 bar. Invisible gold mainly presents in the form of solid solution in all pyrite types. Solid solution gold is also closely related to pyrite2b as the measured Au concentrations in pyrite2b (up to 27 ppm) exceed those in other pyrite types (<0.6 ppm) by one or two orders of magnitude. The

elevated content of invisible Au (together with As, Ag, Zn, and Sb) in pyrite2b is potentially associated with lattice dislocations.

The Re–Os isochron age of pyrite2b (99 ± 10 Ma) and the zircon U–Pb dating of the volcanic and subvolcanic rocks (95.1–104 Ma) indicate that the formation of gold mineralization and the igneous activity in the DVB were coeval during the Turonia–Albian. Geochronology, fluid characteristics, together with low Ni concentrations (<98 ppm) and high mean Co/Ni ratios (≥2.0) of pyrite from different generations, support that the Dongji and Maluntou gold deposits formed in a magmatic-hydrothermal ore system and have an intermediate-sulfidation epithermal origin.

Keywords: Intermediate sulfidation ore system · Pyrite Re–Os isotopes · Gold · Dongkeng Volcanic Basin · SE China

1. Introduction

The Cretaceous epoch, specifically between ~110–90 Ma, was a period of intense magmatic-hydrothermal activity in the South China Block, which was associated with the large-scale lithospheric extension and crust-mantle interaction (Li, 2000; Mao et al., 2008). One of the most important economic manifestations of this activity is the formation of an epithermal gold metallogenic belt along the Southeastern China Fold Belt (SCFB, Fig. 1a). Over twenty-two epithermal gold deposits have been currently explored, possessing a total resource of ~480 t Au (Zhong et al., 2017a) and significant amount of Ag, Cu, Pb, and Zn (Jiang et al., 2017; Wang et al., 2017; Zhong et al., 2017b). Ore-related granites and volcanic/subvolcanic rocks have been dated at 97–114 Ma and 149–158 Ma based on U–Pb, Rb–Sr, and Ar–Ar isochron ages (Yu et al., 2013; Zeng et al., 2013; Li, 2016). They generally possess calc-alkaline or high-K calc-alkaline A- or I-type granite affinities and show the characteristics of igneous rocks related to continental arc or arc-back tectonic settings (Li et al., 2011; Li,2016). By contrast, the origin of these epithermal gold deposits and their possible genetic links to magmatism remain unclear due to the lack of reliable ages and definitive fluid inclusion and geochemistry data, though limited previous studies proposed that most of these deposits are potentially temporal associated with Cretaceous magmatism (Li et al., 2011; Zeng et al., 2013; Jiang et al., 2017; Chen et al., 2020).

Located in the northeastern SCFB, the Dongkeng Volcanic Basin (DVB) with an area of ca. 310 km^2 has developed more than seven operational gold deposits, such as the Dongji, Maluntou, Shangshangang, Baoyan, and Shangshan (Fig. 1c; Chen et al., 2020). Orebodies in these deposits are mainly hosted by volcanic and/or subvolcanic rocks and related to quartz vein systems and various styles of mineralized breccias (Wang, 2013; Lu et al., 2017). Previous studies were controversial about whether magmatic water is involved in the ore system, as the published data of microthermometry and H–O isotopes are heterogeneous. Wang and Yan (2019) proposed that hydrothermal fluids are dominated by meteoric water. Instead, Liu (2016) suggested that ore-forming fluids are more likely derived from the mixture of magmatic and meteoric water. Moreover, there is no reported chronological data on mineralization so far. These lead to the poor understanding of the relationship between gold mineralization and Cretaceous large-scale magmatic activity. Apparently, scientific problems related to ore genesis at the DVB is consistent with that of other similar deposits in the region. Therefore, gold deposits in the DVB are representative and are the ideal objects to study mineralization process. Here, we focus on the Dongji and Maluntou deposits, together with fluid inclusions petrography and microthermometry data to understand the characteristics and evolution of the ore-forming fluids. We also discuss trace element compositions of pyrite from different generations to confirm the correlation between gold and pyrite. Pyrite Re–Os and zircon U–Pb geochronological data are presented to confirm the timing of gold mineralization and magmatism in the DVB. Combined the data contribute to the origin of these gold deposits, and are potentially helpful to improve our understanding of other gold deposits within the SCFB that have similar features to the Dongji and Maluntou deposits.

2. Geological setting

The Dongji and Maluntou deposits are situated in the DVB that is controlled by NE-striking Zhenghe-Dapu fault in the eastern SCFB (Fig. 1). The DVB records multiple volcanic eruptions and subvolcanic events during the Mesozoic period (Guo et al., 2012; Liu et al., 2012). Volcanic rocks in the DVB are divided into an upper and lower series by a regional unconformity (Liu et al., 2016). The lower volcanic series contains the Changlin and Nanyuan formations. The Changlin Formation is mainly composed of conglomerates and sandstones with minor volcanic beds (Fig. A.1). Tuffs of this formation with LA–ICP–MS zircon U–Pb ages of 153–160 Ma (Liu et al., 2016) are the earliest products of Mesozoic volcanism in the region (Liu et al., 2016). The Nanyuan Formation comprises abundant acidic lava and pyroclastic rocks and formed between 141–143 Ma (Guo et al., 2012; Liu et al., 2016). The upper volcanic series, known as the Huangkeng and Zhaixia formations, is the most important host-rocks for the majority of gold deposits within the DVB. The Huangkeng Formation is dominated by volcanic breccia, ignimbrite, and rhyolite, with some sandstone at the base of the succession (Feng et al., 2016). Previous geochronology of the Huangkeng Formation in eastern SCFB is between 100 ± 1 and 112 ± 1 Ma (Guo et al., 2012; Liu et al., 2016). The Zhaixia Formation possesses rock associations ranging from dacite to rhyolite, interlayered with volcaniclastic units (Fig. A.1). This formation yields U–Pb zircon ages of 93.8 ± 1 to 101 ± 1 Ma (Xu, 2011; Guo et al., 2012; Liu et al., 2012; Jiang et al., 2015; Liu et al., 2016) and marks the cessation of volcanism in the DVB. Both the Huangkeng and Zhaixia formations are intruded and, locally, thermally metamorphosed by the Xiaoshao syenogranite porphyry (Fig. 1c). No documented chronological date of this subvolcanic intrusion is known, but gold mineralization within the DVB is suggested to be associated with the emplacement of the Xiaoshao syenogranite porphyry (Feng et al., 2016). In addition, the Xiaoshao syenogranite porphyry locally exhibits intensive limonitization, sericitization, and chloritization alteration with low Au grades (0.5−2.4 g/t), and is considered to be a promising geological unit for the exploration of porphyry Au–Ag mineralization (Feng et al., 2016).

Four generations of faulting are identified in the Dongkeng district. Chronologically these are: 1) NE–SW striking strike-slip faults associated with orebodies (e.g., the Dongji deposit); 2) NW–SE striking faults also associated with orebodies (e.g., the Maluntou deposit); 3) a second generation of NW–SE striking strike-slip faults that are bereft of mineralization and cut all ore-bearing NE–SW striking faults (Fig. 2a); and 4) a second generation of NE–SW striking strike-slip faults.

3. Geology and Mineralization of the Dongji and Maluntou deposits

Gold was first discovered in the Dongkeng district in 1981 and led to the development of commercial mine workings in northern SCFB. Over seven gold deposits and numerous gold occurrences are developed in the DVB, mostly hosted by the upper volcanic series (Fig. 1c). The two largest deposits, i.e., Dongji and Maluntou, that are representative of the geology observed at a large number of artisanal workings were investigated in this study.

3.1. Dongji gold deposit

The measured resource of Au at the currently explored Dongji deposit is more than 12.5 t, including seven principal orebodies with an average grade of 4.27 g/t (Lu et al., 2017). The dominant hosts to orebody are the Jurassic Changlin Formation (ca. 153–160 Ma; Liu et al., 2016) and a rhyolitic porphyry (154 ± 2 Ma; Xiao and Ban, 2015) (Fig. 2). The majority of gold orebodies are structurally controlled (Liu, 2011) and occur as sulfide-bearing quartz veins with occurrence of ca. 1.0-km-long and ca. 30-m-wide (up to 45-m), NE-striking (30–60°) and SE-dipping (30–40°) (Fig. 2a, c). A few less continuous quartz ± calcite pyrite veins with chlorite (± pyrophyllite) alteration selvage are observed proximal to the boundaries of fault zone. They mostly fill in a series of fracture cleavages oriented subparallel or oblique (with a small angle) to the fault zone. Additionally, various styles of breccia mineralization (e.g., crackle breccia and breccia veins) are associated with vein systems. A granite porphyry dike (95.1 ± 0.7 Ma; Fig. 6h) cuts the orebodies, and therefore postdates the gold mineralization.

3.2. Maluntou gold deposit

The Maluntou deposit is located at ca. 4km northeast of the Dongji deposit and ca. 3 km north of the Xiaoshao syenogranite porphyry (Fig. 1c), has been explored by the Minbei No. 1

Geological Team (No. 1 G.T.) since 2003. The identified recoverable gold resource is more than 5.0 t with an average grade of 3.7 g/t (Liu, 2017). The ore system is hosted by hydrothermally altered volcanic breccia and dacitic-rhyolitic volcaniclastic rocks of the Huangkeng Formation. Ten subparallel lodes (thickness 1–3 m) and 21 smaller lenticular veins (thickness <1 m) are recognized at 66–600 m elevations. Similar to the Dongji deposit, orebodies in the Maluntou deposit are also spatially associated with the fault system (Fig. 2b), e.g., the tensional NW-striking (310–342°) faults and fractures. The Au2 lode (ca. 420 m in length and 4–19 m in width) is the largest lode that dips at 60–80° northeast (Fig. 2d). Other lodes exhibit a similar orientation. The exception is a few lodes located at northeastern end of the Maluntou deposit (e.g., Au12, Au13, and Au14) that dip at 66–74° northwest (Liu, 2017). Three alteration zones are recognized in the ore system, especially in proximity to Au2 lode, ranging from silicification + sericite, silicification + chlorite, and chlorite + argillic alteration from the centre of ore-vein outwards to the host-rocks (Fig. 2d).

3.3. Paragenetic sequence and mineralization stages

Ores in the Dongji and Maluntou deposits are similar, consist of multiple vein phases filled by microcrystalline to coarse-grained quartz and sulfides. Sulfide mineralogy is relatively simple and consists of pyrite with arsenopyrite, chalcopyrite, galena, and sphalerite (Liu, 2011; Lu et al., 2017). Nevertheless, the genetic significance of mineral associations is tentative, as all of the observed fault-fill quartz veins, indicators of a vein history, locally possess complex crosscutting relationships and suggest three stages of mineralization (e.g., Figs. 3 and 4).

Stage 1: Quartz veins in this stage are characterized by quartz-pyrite-arsenopyrite assemblage with chlorite-K-feldspar alteration selvages (Figs. 3a, 4a). Quartz veins are typically ca. 10–50 cm wide and occur at 66–600 m elevations. Quartz (quartz1) is generally medium- to coarse-grained (>1 mm) white euhedral-subhedral crystal, and exhibits bright brown fluorescence with growth zones in cathodoluminescence images (Fig. A.2). Euhedral to subhedral pyrite (pyrite1, <1 mm) and arsenopyrite are disseminated within quartz veins. Arsenopyrite is generally enveloped by pyrite1 (Fig. 5a). Free gold is not recognized visually or petrographically.

Stage 2: Quartz veins (Figs. 3b–i, 4b–d) are closely associated with polymetallic sulfide mineralization, as well as gold mineralization in the Dongji and Maluntou deposits. Quartz veins predominantly occur between 250 and 500 m elevations and are associated with intensive alteration phases, e.g., sericite, chlorite, and clay minerals. Individual veins generally exhibit complex patterns (Fig. 3b) and distinctive grey coloration caused by fine-grained (<0.5 mm) smoky gray anhedral quartz crystals and sulfide-bearing bands. Quartz (quartz2) in this stage is significantly different from the one in the stage 1. Quartz2 exhibits blue fluorescence without growth zones (Fig. A.2) and locally surrounds quartz1 or fills fractures within quartz1. Pyrite, visible gold, chalcopyrite, galena, and sphalerite are diagnostic component of quartz veins (Fig. 5b–d). Two types of pyrite are recognized, including cubic, fine-grained (<0.3 mm) pyrite (pyrite2a) and aggregates of pyrite (pyrite2b, <1.5 mm) with porous texture and corroded edges. Pyrite2b is significantly more abundant than that of pyrite2a (typically pyrite2b represents >95 % of the total pyrite abundance in the stage 2 veins). Pyrite2a is generally enveloped by pyrite2b (Fig. 5b, g). In turn, pyrite2b is replaced by chalcopyrite, sphalerite, and galena as rims and fracture fillings (Fig. 5c–d). Visible gold shows a close relationship with pyrite2b, mainly forms micrometer-sized inclusions of native gold and electrum within crystal interstices, fractures, and hollows of pyrite2b (Fig. 5c, g). Textural evidence suggests that gold is coeval with or locally postdates pyrite2b deposition.

Stage 3: Quartz veins (Figs. 3j–k, 4d) predominantly occur at shallow levels (elevations greater than ~300 m) and are associated with calcite veins. Quartz (quartz3) occurs as fine-grained (<0.5 mm) white anhedral crystal quartz and comb quartz without any fluorescence (Fig. A.2). Sulfides are largely absent, as well as gold, with the exception of disseminated coarse (>1 mm) euhedral pyrite (pyrite3; Fig. 5e). Green and purple fluorite can be observed in some veins at 360 m elevation.

4. Samples and methods

4.1. LA–ICP–MS zircon U–Pb geochronology

Hydrothermally unaltered / least altered samples, including the rhyolitic ignimbrite of the Huangkeng Formation, the rhyolite of the Zhaixia Formation, the Xiaoshao syenogranite porphyry and the post-mineralization granite porphyry dike, were collected for LA–ICP–MS U–Pb zircon dating. The detailed sample locations are listed in Table A.1 and shown in Figs. 1c and 2a.

The rhyolitic ignimbrite sample (HK-1) is characterized by pyroclastic material (>70 %), quartz and feldspar phenocrysts (10−20 %), and pseudo flow texture (Fig. 6a). The matrix is dominated by volcanic ash, and microcrystalline feldspar and quartz. The rhyolite sample (ZX-1) shows clear flow texture and comprises quartz (10−20 vol%) and K-feldspar (5−10 vol%) phenocrysts, with a predominantly cryptocrystalline matrix (Fig. 6b). The Xiaoshao syenogranite porphyry has a porphyritic texture. Phenocrysts are characterized by orthoclase (30−35 vol%) with minor biotite (<5 vol%) and hornblende (<5 vol%). The matrix is dominated by microcrystalline feldspar such as orthoclase and plagioclase. The collected sample (XS-1) possesses minor sericitization (Fig. 6c). The post-mineralization granite porphyry dike sample (DJ-1) shows a similar mineral compositions to that of the Xiaoshao syenogranite porphyry, but phenocryst is dominated by K-feldspar rather than orthoclase (Fig. 6d).

Zircon from the collected whole rock samples were separated at the Laboratory of the Langfang Regional Geological Survey Institute, Hebei Province, China, using traditional separation methods (i.e., combination of heavy liquid and magnetic separation techniques, followed by handpicking under a binocular microscope). To study the morphology and internal structure of separated zircon, reflected and transmitted light microscopy and cathodoluminescence (CL) observations were carried out at the electron microprobe laboratory in the State Key Laboratory of Geological Processes and Mineral Resources (GPMR), China University of Geosciences, Wuhan.

Guided by CL images, zircon U–Pb isotopes were measured on an Agilent 7500 ICP–MS equipped with a 193 nm laser at the GPMR following published analytical procedures (Liu et al., 2008). Spot laser ablation of 32 μm and laser pulse repetition frequencies of 8 Hz were utilized. Off-line inspection, integration of background and analyzed signals, time-drift correction and quantitative calibration for U–Pb dating were performed using *ICPMSDataCal* (Liu et al., 2008). Concordia diagrams and weighted mean calculations were made using Isoplot/Ex_ver 4.15 (Ludwig, 2008).

4.2. ID–N–TIMS Pyrite Re–Os

Texture evidence shows a close relationship between native gold and pyrite2b. In this case, seven pyrite samples from the stage 2 veins were selected to constrain the timing of gold mineralization. All samples were collected from the Au1 orebody (at 416 m elevation) of the Dongji deposit. Some samples were divided into two fractions (Fig. 3), thus there were a total of 10 pyrite separates. The detailed sample locations are shown in Fig. 2c and Table 1. In hand specimens, pyrite is mostly massive (Fig. 3) with the exception of sample DK-LP-34 that possesses disseminated pyrite (Fig. 3h). Microscopic observations show that the pyrite is predominantly pyrite2b (>98 %) with only minor pyrite2a (Fig. 5b-d). About 1 g of each pyrite separates was obtained using traditional isolation methods (i.e., crushing, magnetic, and/or heavy liquid separation and handpicking).

The pyrite Re–Os analyses were conducted at the Source Rock and Sulfide Geochronology and Geochemistry Laboratory in the Durham Geochemistry Centre at Durham University. The analytical protocol follows that documented by Selby et al. (2009). In brief, 400 mg of each separates was dissolved and equilibrated with a known amount of a mixed Re–Os tracer solution (^{185}Re + ^{190}Os) by inverse aqua regia (3 ml of 11 N HCl and 6 ml of 15.5 N HNO_3) in a carius tube for 24 h at 220 °C. Osmium was isolated and further purified from inverse aqua regia by $CHCl_3$ solvent extraction and microdistillation. Rhenium was isolated using anion column chromatography methods. The purified Re and Os were loaded onto the degassed Ni and Pt filaments, respectively, and analyzed using negative thermal ionization mass spectrometry (Creaser et al., 1991; Völkening et al., 1991) on a Thermo Scientific TRITON mass spectrometer at the Arthur Holmes Laboratory at Durham University. The Re was measured using static Faraday collectors and Os in peak-hopping mode using a secondary electron multiplier.

Total procedural blanks were monitored during the course of study. Blanks for Re and Os were 4.06 pg and 0.36 pg, with an average $^{187}Os/^{188}Os$ value of 0.19 ± 0.04 (1SD, n = 3). The operational conditions of the spectrometer were monitored by reference solutions DROsS and Re standard (Selby and Creaser, 2001). The $^{187}Os/^{188}Os$ values of DROsS are 0.16087 ± 0.00026, with the $^{185}Re/^{187}Re$ values of the Re standard being 0.5993 ± 0.0006 (1SD, n = 3). These measured values are in good agreement with those previously reported at Durham University (e.g., Saintilan et al., 2018 and references therein). Analytical uncertainties are propagated and incorporate uncertainties related to Re and Os mass spectrometer measurements, blank abundances and isotopic compositions, spike calibrations, sample weights, and reproducibility of standard Re and Os isotope values. The Re–Os data of this study were regressed using the program Isoplot/Ex_ver 4.15 (Ludwig, 2008).

4.3. In-situ trace element analysis of pyrite by LA–ICP–MS

Trace element analyses of four pyrite types were conducted by LA–ICP–MS at the Wuhan Sample Solution Analytical Technology Co., China. Detailed operating conditions for the laser ablation system and the ICP–MS instrument and data reduction are the same as those described by Zong et al. (2017). Laser sampling was performed using a GeolasPro laser ablation system that consists of a COMPexPro 102 ArF excimer laser (wavelength of 193 nm and maximum energy of 200 mJ) and a MicroLas optical system. An Agilent 7700e ICP–MS instrument was used to acquire ion-signal intensities. Helium was used as the carrier gas. Argon was used as the make-up gas and mixed with the carrier gas via a T-connector before entering the ICP. A "wire" signal smoothing device is included in this laser ablation system (Hu et al., 2014). The spot size and frequency of the laser were 32 μm and 5 Hz, respectively. Trace element compositions of pyrite were calibrated against various reference materials (NIST 610 and NIST 612) without using an internal standard (Liu et al., 2008). The sulfide reference material of MASS-1 (USGS) was used as the unknown sample to verify the accuracy of the calibration method. Each analysis incorporated a background acquisition of approximately 20–30 s followed by 50 s of data acquisition from the sample. The trace element data of pyrite were calculated using an Excel-based software *ICPMSDataCal* (Liu et al., 2008).

4.4. Microthermometry and Laser Raman Spectroscopy

Thirteen quartz samples corresponding to the three mineralization stages were collected to study fluid inclusions, all of which came from the underground mining laneway at the elevation of ca. 100–400 m. Among these samples, eight were from the Au1 ore-body of the Dongji deposit, and the rest were from the Au17 ore-body of the Maluntou deposit. The details of sample location are shown in Table 2. The microthermometric measurements of fluid inclusions in this study were mainly focused on fluid inclusion assemblages (FIAs) that were defined as fluid inclusion vacuoles along the same growth zone in a single crystal or along a single intra-grain fracture/crack (Fig. 8). The examined 13 FIAs (Table 2) consist of primary and pseudosecondary fluid inclusions that occur as clusters and short trails (Fig. 8). Individual fluid inclusions generally possess a diameter between 6 and 10 μm with round to sub-round or polygonal in shape.

Microthermometric analyses were carried out at the Geofluids Research Laboratory, China University of Geosciences, Wuhan, using a Linkam THMS600 heating-freezing stage on an Olympus transmitted light microscope. The precision of freezing runs was ±0.2 °C and of heating runs was ±2 °C. Synthetic fluid inclusion standards (pure CO_2 and pure water) were used (Baumgartner et al., 2014) to calibrate the stage. The volumetric fraction of phases in fluid inclusions was estimated at room temperature by reference to the volumetric chart of Roedder (1984). Bulk salinity was calculated using the equations of Bodnar (1993) and are shown graphically in Fig. 9, along with homogenization temperatures. The homogenization condition (e.g., density and capture pressure) of individual FIAs was calculated by Flincor H_2O–NaCl program based on fluid inclusion volumetric data (Brown and Hagemann, 1995).

Gas phases from selected fluid inclusions were identified using a JY/Horiba LabRam HR800 system at Key Laboratory of Tectonics and Petroleum Resources, Ministry of Education, China University of Geosciences, Wuhan. Sample excitation was achieved using a Ventus diode-pumped, continuous wavelength, 532.06 nm laser with a maximum power output of 45 nW. The detector charge-coupled device area is 20 μm^2, and the scanning range for spectra was set between 1000 and 4000 cm^{-1}, with an accumulation time of 30 s for each scan.

5. Results

5.1. LA–ICP–MS zircon U–Pb age

All analytical spots were located on pale, euhedral and prismatic zircon grains with clear CL zonation (Fig. 6). The zircon morphological and textural features confirm a magmatic origin. The U–Pb data of the studied volcanic and subvolcanic rocks are listed in Table A.1 and illustrated in Fig. 6.

For the rhyolitic ignimbrite (HK-1) of the Huangkeng Formation, 23 analyses yield a weighted mean $^{206}Pb/^{238}U$ age of 104 ± 0.7 Ma (MSWD = 1.8; Fig. 6e). This age is in good agreement with previous published data (100–112 Ma, Guo et al., 2012; Liu et al., 2016) in the region. Twenty-one spot analyses for the rhyolite sample (ZX-1) show a slightly younger weighted mean ^{206}Pb/^{238}U age of 101 ± 0.4 Ma (MSWD = 0.7; Fig. 6f), representing the formation age of the Zhaixia Formation. For the Xiaoshao syenogranite porphyry, ^{206}Pb/^{238}U ages obtained from 21 analyses range from 99 ± 4 to 102 ± 3 Ma, yielding a weighted mean ^{206}Pb/^{238}U age of 101 ± 0.6 Ma (MSWD = 0.6; Fig. 6g). In combination with the oscillatory zoning of zircon, this age is interpreted as the crystallization age. For the granite porphyry dike, 19 spot analyses form a near coherent cluster and yield a weighted mean age of 95.1 ± 0.6 Ma (MSWD = 2.1; Fig. 6h). This result provides the youngest possible age (i.e., ca. 95 Ma) for the timing of gold mineralization in the DVB, as the granite porphyry dike crosscuts the orebodies.

5.2. Pyrite Re–Os data

Blank-corrected Re–Os data of ten pyrite2b dominated separates are reported at the 2 sigma level uncertainty in Table 1 and are graphically presented in Fig. 7. Eight of ten separates have Re concentrations of ca. 1 ppb. The remaining two separates (DK-LP-34 and DK-LP-7) contain only 0.06 and 0.1 ppb Re. Total Os concentrations in all samples are low, ranging from 4 to 41 ppt. Differing from the typical "low level highly radiogenic" sulfides that are characterized by low Re and Os concentrations, high radiogenic Os isotope compositions (^{187}Os^{r}, typically greater than 90 %) and high ^{187}Re/^{188}Os ratios (>5000) (Stein et al., 2000), pyrite in this study shows low ^{187}Os^{r} values (<73 %) and ^{187}Re/^{188}Os ratios (<1693) (Table 1). This suggests a significant common Os component and indicates that individual model age calculations are not applicable (Stein et al., 2000). The regression of ^{187}Re/^{188}Os versus

$^{187}Os/^{188}Os$ compositions yields a Model 3 data (assumes that the scatter about the best-fit line is due to a combination of the assigned uncertainties, and an unknown but normally distributed variation in the $^{187}Os/^{188}Os$ values; Ludwig, 2008) of 139 ± 14 Ma (N = 10, MSWD = 216; Fig. 7a), with an initial $^{187}Os/^{188}Os$ (Osi) value of 0.36 ± 0.26.

5.3. Fluid inclusions

Fluid inclusion petrography Fluid inclusions in quartz veins are classified into four types based on the estimated volumetric proportions of the phases present at room temperature, phase transitions during heating and cooling runs, and laser Raman spectroscopy. These are: Type1 – liquid-rich two-phase inclusions (the volume percentage of vapor is 0−30 vol%, Fig. 8d); Type2 – liquid-vapor two-phase inclusions (30−60 vol%, Fig. 8e); Type3 – vapor-rich two-phase inclusions (60−100 vol%; Fig. 8f); Type4 – saline inclusions (i.e., halite-bearing fluid inclusions with or without sylvite daughter crystal; Fig. 8g–i).

Traces of gases such as CO_2 are not observed by clathrate melting nor are they detected by laser-Raman spectroscopy in vapor bubbles of type1, 2, and 3 inclusions (Fig. 8). The only nonelectrolyte in these inclusions is H_2O, suggesting that fluids are approximated by H_2O–NaCl system. In addition, halite in saline inclusions is identified by cubic form and optical isotropy (Fig 8g–i), with sylvite being distinguished from halite by its round form and lower relief (Fig 8g, h).

Microthermometry The majority of fluid inclusions homogenize to the liquid phase with the exception of type3 and a few type2 inclusions that are homogenized by the vapor phase. The results of the microthermometric data are summarized in Table 2, and plotted in Fig. 9.

In the stage 1 quartz (quartz1), FIAs are dominated by type1 and type2 inclusions and show a broad range in homogenization temperatures (308−377 °C) but a small variation in salinities (4.6−9.1 wt% NaCl equiv.) (Fig. 9).

In the stage 2 quartz (quartz2), FIAs are generally two-phase inclusions (e.g., Nos. 5'', 6, 7, 8, and 9 FIAs; Fig. 9) that share similar salinities (3.2−9.1 wt% NaCl equiv.) to the stage 1 fluids, but possess slightly lower homogenization temperatures (253−341 °C, predominantly between 295 and 340 °C). In addition to two-phase inclusions, a small amount of saline inclusions are measured. The dissolution of halite in these type4 inclusions generally occurs earlier than bubble disappearance. Type4 inclusions (i.e., No. 5' FIAs) show final homogenization temperatures of 345−374 °C with exceedingly high salinities of 40.4−42.4 wt% NaCl equiv. (Fig. 9).

In the stage 3 quartz (quartz3), fluid inclusions (e.g., Nos. 10−13 FIAs) are homogenized into the liquid phase at temperatures of 198−329 °C, with low salinities between 1.0 and 6.5 wt% NaCl equiv. (Fig. 9c). The mean values of homogenization temperature (ca.240 °C) and salinities (ca. 3.8 wt% NaCl equiv.) of fluid inclusions are slightly lower compared to those of stage1 and 2 veins, indicating distinct cooling and dilution of the hydrothermal system.

5.4. Trace element characteristics of pyrite

A total of 68 spot analyses were conducted on the pyrite set, including 14 spots on pyrite1, 18 spots on pyrite2a, 31 spots on pyrite2b, and 5 spots on pyrite3. A summary of trace element concentrations is given in Table 3. The full dataset is given in Table A.2. The concentration of trace elements is illustrated by boxplots (Fig. 11).

The time-resolved LA–ICP–MS profiles (i.e., time vs. intensity) of Au, Cu, Pb, Zn, Ag, and Sb of all analyzed pyrite are fluctuating (i.e., with spikes), although they remain at a relatively high level (Fig. 10). However, the signal of As is relatively smooth and steady. A parallel pattern between As and Au is yielded from most pyrite (Fig. 10a, c), especially in pyrite2b. In addition, the signals of Co and Ni are generally consistent with those of Fe and S (Fig. 10), supporting that these siderophile elements are commonly distributed in different pyrite types via isomorphism (Zhao et al., 2011).

Elements such as Co, Ni, Au, Cu, Zn, As, Ag, Sb, Pb, Mn, Bi and Ti are presented to show similarities and differences between four pyrite types, as the concentration of these elements is largely above the minimum detection limits (Table 3). Pyrite1 shows a narrow range in trace element concentrations with the exception of Ti (Fig. 11). The median Au content of pyrite1 is 0.1 ppm (Table 3). Pyrite2a contains a wider range of trace elements at measurable concentrations compared to pyrite1, notably Cu, Ag, Pb, Zn, and Sb (Fig. 11). The Au concentration of pyrite2a is also low (<0.2 ppm). Pyrite2b can be clearly distinguished from other pyrite types as pyrite2b is relatively enrichment in Au (<0.04 to 27 ppm). The concentration of other elements in pyrite2b, Co, Ni, As, Ag, Zn, Sb and Cu in particular, is also higher than those of other pyrite types (Fig. 11). Pyrite3 shows a similar trace element distribution pattern to that of pyrite1, with Au concentration less than 0.5 ppm.

6. Discussion

6.1. Fluid characteristics and evolution

Fluid inclusions hosted in the stage 1 quartz (quartz1) show intermediate-density, homogenization temperatures well above 310 °C, and salinities below 10 wt% NaCl (Fig. 9). These characteristics are comparable to those of fluids in some magmatic-hydrothermal systems (e.g., porphyry, high- and intermediate-sulfidation epithermal, and hydrothermal vein-type; Heinrich et al., 2004; Redmond et al., 2004). The fluids in these magmatic-hydrothermal systems generally possess a magmatic origin (Zhong et al., 2017b; Chang et al., 2018). In addition, the constant decrease in temperatures with minor change in salinities of the stage 1 hydrothermal fluids (Fig. 9) suggests a cooling process and is commonly observed in proximal hydrothermal systems related to magmatic intrusions (e.g. Hedenquist and Lowenstern, 1994)

The low-salinity fluids (3.2−9.1 wt% NaCl equiv.) characterized by moderate temperatures of 295−340 °C are recorded by abundant two-phase inclusions (Fig. 9) in the stage 2 quartz veins. This indicates that low-salinity fluids dominate in the stage 2 hydrothermal fluids and are probably responsible for the deposition of most ore minerals. Texture evidence also supports that quartz2 and sulfides (e.g., pyrite2b, galena, and sphaerite), and by inference the gold, formed from the homologous fluids. In figure 9 temperatures of low-salinity fluids of the stage 2 are slightly lower than those of the stage 1 fluids (Fig. 9), but are broadly consistent with those of the epithermal deposits, in particular of gold-precipitation-stage in most intermediate-sulphidation depoists (e.g., wang et al., 2019). Liquid-rich inclusions in quartz2 commonly coexist with vapor-rich inclusions, e.g., No. 6 FIAs (Fig. 9) and share similar homogenization temperatures and salinities (Table 2). This indicates that low-salinity fluids of the stage 2 intersected the solvus and boiled to form low-density vapors (Driesner and Heinrich, 2007). The occurrence of various styles breccia mineralization (e.g. crackle breccia, breccia veins) along some stage 2 quartz veins is also accepted as evidence of boiling (Canet et al., 2011). In this case, fluid characteristics shown by No. 6 FIAs (i.e., boiling inclusions with salinity of ~5 wt% NaCl and homogenization temperature of ca. 329 °C), coupled with a pure H_2O−NaCl system (Fig. 8), the entrapment pressure for the stage 2 low-salinity fluids is calculated to be approximately 120 bar (Driesner and Heinrich, 2007).

Apart from low-salinity fluids, high-salinity fluids (>40 wt% NaCl equiv.) are recorded by a small amount of saline inclusions in the stage 2 veins (Fig. 9). The absence of coexisting saline inclusions and vapor-rich inclusions makes it plausible to rule out the role of fluid immiscibility (Heinrich et al., 2004). In addition, homogenization temperatures of saline inclusions (>345 °C) are higher than those of other fluid inclusion types (<340 °C) in the stage 2 veins (Fig. 9). Given that most of saline inclusions are homogenized by bubble disappearance rather than dissolution of halite, fluid pressure (ca. 125 bar) at the temperature of bubble disappearance (ca. 361 °C; Table 2) generally represents the minimum fluid trapping pressure (Roedder and Bodnar, 1980). This estimated minimum pressure is slightly higher than the ones of the stage 2 low-salinity fluids (ca. 120 bar). By inference, the presence of abundant low-salinity fluids and a much smaller amount of high-salinity fluids during the stage 2 may be related to the pressure fluctuation due to faulting or seismic pumping (Roedder and Bodnar, 1980). This is consistent with the observation that the mineralization at the Dongji and Maluntou is apparently associated with fault systems (Fig. 2) and the development of comb structures in quartz veins (Fig. A.2). The faulting or seismic pumping mechanism may have caused inflow of fluids with different characteristics (Sibson et al., 1988). In fact, faulting or seismic pumping is commonly observed in mesothermal gold-quartz deposits formed at high pressure about 2 to 4 kbar (Sibson et al., 1988), whereas Chi et al. (2017) suggested that such process could also occur in a shallow environment (<200 bar).

The formation of quartz3 associated with calcite and pyrite3 marks a waning stage of the hydrothermal system. Quartz3 deposited from the late-stage (stage 3) fluids with low temperatures (220−250 °C) and low salinities (1.0−6.5 wt% NaCl equiv.) (Fig. 9). Such temperatures and salinities are similar to the ones of fluids in typically low-sulfidation epithermal system within the SCFB, which possess a mixed origin of magmatic and meteoric water (Zhong et al., 2017b). In addition, the larger temperature difference (~43 °C) between each FIAs within the stage 3 veins compared to ~24 °C shown in other mineralization stage veins potentially supports a rapid cooling process related to the collapse of the heat system and incursion of near-surface meteoric water (Hedenquist and Lowenstern, 1994).

Overall, the hydrothermal fluids in ore system are dominated by low salinity fluids. Fluid inclusions from the stage 1 quartz veins are most likely to represent the initial fluids that potentially have a magmatic origin. These initial fluids possess moderate temperatures (308−377 °C) and low salinities (4.6−9.1 wt% NaCl equiv.). Subsequently, fluid boiling took place at pressure of ca.120 bar and most sulfides precipitated during the deposition of quartz2, forming the stage 2 sulfide-bearing quartz veins. The temperatures of boiling fluids (295−340 °C) decreased from the initial fluids but the salinities were still low (3.2−9.1 wt% NaCl equiv.). Finally, the fluids characterized by lower temperatures (220−250 °C) and lower salinities (1.0−6.5 wt% NaCl equiv.) may be related to the mixing of magmatic and meteoric water and then formed the quartz3 in the late-stage veins.

6.2. Correlation between gold and pyrite

Both invisible gold and visible gold occur in the Dongji and Maluntou deposits.

Invisible gold and pyrite LA–ICP–MS analyses of the four pyrite types from the Dongji and Maluntou deposits yield a positive correlation between Au and As (Fig. 12a), which is consistent with the characteristics of invisible gold-bearing pyrite in epithermal gold deposits (e.g., Cook and Chryssoulis 1990; Sung et al. 2009). A parallel pattern between the signals of As and Au from most pyrite (Fig. 10) also supports the presence of invisible gold. Therefore, the Reich et al. (2005) Au-saturation line in figure 12a could be used to recognize the occurrence of invisible gold (solid solution or nanoparticles; Ciobanu et al., 2012). Apparently, all data fall below the gold solubility limit line (Fig. 12a), suggesting that invisible gold occurs mainly as solid solution (i.e., Au^{1+}) in a structurally bound Au complex within the pyrite lattice. In fact, it needs to be noted that small amount of invisible gold occurring as nanoparticles (e.g., submicroscopic inclusions of discrete Au-bearing phases) cannot be excluded, because the presence of sharp spikes on Au distribution pattern for LA–ICP–MS spot analyses of pyrite2a and pyrite3 (Fig. 10b, d). The positive correlation of Au−As (Fig. 12a) rather than Au−Cu (Fig. 12c) indicates the coupling relationship between Au and As and the insignificant influence of chalcophile elements on the Au concentrations in pyrite (Hazarika et al., 2017). By inference,, substitution of As for Fe or S creates lattice dislocations that facilitate Au^{1+} entering into the crystal structures of pyrite (Cook and Chryssoulis, 1990; Huston et al., 1995; Deditius et al., 2008), which can reasonably explain the lattice-bound form. In addition, the measured invisible Au concentrations in pyrite2b from the stage 2 quartz veins generally exceed those in other pyrite types by one or two orders of magnitude (Table 3), indicating that the stage 2 is the important period of invisible gold precipitation.

Visible gold and pyrite Visible gold mainly forms micrometer-sized inclusions of native gold and electrum within crystal interstices, fractures, and hollows of pyrite2b (Fig. 5) in stage 2 veins. This kind of occurrence of the visible gold is identical to that of the previously reported in the Shuiyindong and Gutaishan gold deposits (Liu et al., 2018; Li et al., 2019). The deposition of visible gold in the Shuiyindong and Gutaishan gold deposits is attributed to the remobilization of invisible gold in earlier formed pyrite (Liu et al., 2018; Li et al., 2019). Such remobilization model (Mumin,1994), however, may be not the case for the visible gold in the Dongji and Maluntou deposits based on the following evidences. Apparently, the insufficient invisible gold content of earlier formed pyrite (less than 1 ppm, Table 3) argues against the remobilization process according to the mass balance grounds (Yang et al., 2016). In addition, pyrite2b shows the homogeneous texture without compositional zoning, which is different from that of the visible gold-bearing pyrite in the Shuiyindong and Gutaishan gold deposits (Liu et al., 2018; Li et al., 2019). The absence of remobilization related minerals (e.g., pyrrhotite or arsenopyrite) coexisting with remobilized pyrite (Fig. 5) is added as a line of unsupported evidence. In such situation, visible gold is more likely to precipitate directly from hydrothermal fluids (Li et al., 2019) and an efficient mechanism must have operated to produce the visible gold. In fact, fluid boiling is commonly observed in porphyry-epithermal and epithermal gold deposits within the SCFB (Zhong et al., 2017b and references therein). Significant loss of the sulfide ligand into the vapor during fluid boiling potentially results in gold saturation and the great precipitation of visible gold (Mikucki, 1998). Fluid boiling has been carefully assessed in the Dongji and Maluntou deposits, and is apparently supported by boiling inclusions assemblages (discussed above), the existence of hydrothermal brecciation related to mineralization and the presence of bladed calcite. By inference, the deposition of visible gold to form the high-grade orebodies in the study area is more likely to be triggered by fluid boiling. The texture relationship between visible gold and pyrite2b (Fig. 5) further suggests the progressive influx of hydrothermal fluids during gold mineralization, as corroded interiors and margins of pyrite2b indicates postdepositional dissolution.

The variation of Au (Ag, As, Zn, Sb) among different pyrite generations Although trace element concentrations in pyrite from different generations show obvious variation, we note that the concentration of Au exhibits an increasing trend from pyrite1, pyrite2a to pyrite2b, and then decreases significantly during pyrite3 precipitation. The similar distribution pattern is also shown by Ag, As, Zn and Sb elements (Fig. 11). Such trend is consistent with that previous reported in the Lihir gold deposit (Sykora et al., 2018). For the Lihir deposit, the low level of most trace elements in the early stage pyrite is related to slow growth rate of pyrite and high solubility of trace elements in aqueous solution due to high temperatures. The suite of trace elements enriched in the middle stage pyrite results from disequilibrium precipitation of pyrite (Sykora et al., 2018).

For the Dongji and Maluntou deposits, temperatures of the stage 1 hydrothermal fluids (up to 377 °C) are comparable with the ones of the Lihir gold deposit (Sykora et a. 2018), probably suggesting a connection between the high-temperature environment and the low concentrations of trace elements in pyrite1. The possible scenario responsible for high concentrations of Au, Ag, As, Zn, and Sb in pyrite2b are various (e.g., temperature, absorption properties of pyrite, fluid composition, precipitation rate, and availability of Fe and/or S; Sykora et al., 2018 and references therein). We suggest that the rapid precipitation of pyrite2b due to fluid boiling probably play a key role, although other parameters should also be carefully considered. Disequilibrium precipitation of pyrite is enhanced under conditions of rapid precipitation (Huston et al., 1995 and references therein), and helps to incorporate trace elements into pyrite as a solid solution (e.g., Au) or as a micro- to nanoscale inclusion (e.g., Ag, Zn, Pb, and Sb). The concentration of most trace elements in pyrite3 decreases evidently compared to that of pyrite2b (Fig. 11), which may imply that the ore-forming elements (e.g., Au) and associated chalcophile elements (e.g., As, Ag, Cu, Pb, Zn, and Sb) in hydrothermal fluids have been consumed during the precipitation of pyrite2b. Additionally, the influx of meteoric water during the late stage of the hydrothermal ore system may further dilute the fluids. In summary, the differences in trace element composition of pyrite from different generations are related to the complicated process, and the close relationship between gold (both invisible and visible gold) and pyrite2b is well defined.

6.3. Timing of gold mineralization

Previous geochronology, on the bases of Rb−Sr (on quartz and whole-rock), K−Ar (on alunite, sericite, and adularia), Ar−Ar (on alunite and adularia), Re−Os (on molybdenite) and TIMS U−Pb (on zircon) dating methods, shows that gold mineralization in the SCFB are of Oxfordian-Toarcian (ca. 157−181 Ma) and Turonian-Albian (ca. 91−110 Ma) (Li, 2016; Zhong et al., 2017b and references therein). In the DVB, the indirect timing constraints of gold mineralization are given by the age of host-rocks and post-mineralization dikes. For example, the age of 104 ± 2 Ma (Fig. 6) obtained from the rhyolitic ignimbrite (in which orebodies in the Maluntou deposit are hosted, Fig. 1c) indicates a maximum date for mineralization at Maluntou. Similarly, the rhyolitic porphyry (154 ± 2 Ma; Xiao and Ban, 2015) hosting orebodies in the Dongji deposit (Fig. 2a), together with a post-mineralization granite porphyry dike (95.1 ± 0.7 Ma; Fig. 6) bracket the timing of gold mineralization at Dongji between Cenomanian and Tithonian.

All of the Re−Os data of pyrite2b dominated separates from the stage 2 veins in the Dongji deposit yield a Model 3 age of 139 ± 14 Ma (N = 10, MSWD = 216, initial $^{187}Os/^{188}Os$ [Osi] = 0.36 ± 0.26; Fig. 7a). This date within the uncertainty broadly conforms to that of geological constraints (ca. 95−154 Ma) from the host-rocks and post-mineralization dikes, but is not compatible with time patterns of gold mineralization in the region. The percentage of deviation from the best-fit line of all of the Re−Os data is illustrated in Fig. 7b, which shows that six of ten pyrite separates (DK-LP-5, -7, and -34, DK-JX-351, -353, and -354) exhibit a deviation greater than 5 % and up to 50 %. A Model 3 age, large uncertainty, an MSWD much higher than 1, and significant deviation from the best-fit line suggest that scatter about the linear regression is related to geological factors rather than purely analytical uncertainties (Ludwig, 2008). For example, the entire sample set does not represent contemporaneous formation, or possess identical Osi, or that the Re−Os isotope system has been disturbed (Stein et al., 2000; Selby et al., 2007; Cumming et al., 2014). Calculating the Osi for each pyrite separates at 139 Ma (Osi_{139}), which is based on the Re−Os date of all separates, shows that the Osi values are heterogeneous (0.11−0.65; Table 1). Therefore, we suggest that the variation in the Osi may be a potential cause of scatter about the best-fit line.

As stated above, the ca.139 Ma date is obtained from pyrite separates with variable Osi. Therefore, a Re−Os date based on homogeneous Osi compositions was attempted to yield in this study. When the Osi values are calculated at 95 Ma (which is the youngest possible for mineralization based on the emplacement age of the post-mineralization granite porphyry dike in the Dongji deposit), distinct Osi data clusters are evident (Table 1). Six of ten samples possess similar Osi_{95} of 1.41−1.51, with the remaining samples possessing lower and dispersed Osi_{95} of 0.28−0.70 (N = 4). Calculation of the Osi at 110 Ma (representing the oldest known gold mineralization time in the region; Zhong et al., 2017b) yields a similar outcome (Table 1). For example, six samples yield Osi_{110} values of 1.01−1.17, with the remaining samples showing scattered Osi_{110} values of 0.26−0.68 (N = 4). The difference in Osi clusters may be related to samples that include different generation ages or have experienced disturbance to the Re–Os isotope system (Stein et al., 1998; Schaefer et al., 2010). The Osi_{95} and Osi_{110} data demonstrate that the calculation at an older age yields slightly less radiogenic Osi (Table 1), but this does not change the relationship of pyrite separates to each other and therefore does not adversely affect geochronology based on the Osi composition (Cumming et al., 2014).

Regression of the Re–Os data based on Osi data groupings, six pyrite separates characterized by similar and high Osi (>1) yield a Model 1 (which considers that only the assigned uncertainties produce the scatter about the best-fit line; Ludwig, 2008) Re–Os date of 99 ± 10 Ma (MSWD = 0.47, Osi = 1.35 ± 0.26; Fig. 7c). The remaining four samples with lower and scattered Osi (<0.7) do not give a valid isochron. The age of 99 ± 10 Ma agrees well with the general temporal understanding of gold mineralization (91−110 Ma) in the SCFB (Zhong et al., 2017b and references therein). The data also enters the indirect gold mineralization age window (<ca. 104 Ma; Fig. 6) indicated by host-rocks in the Maluntou deposit. Therefore, although the data shows large uncertainty, it is considered to represent the best estimate for the timing of gold mineralization in this study. The large age uncertainty

may be related to the variability in the Osi (Osi_{99} = 1.32–1.41; Table 1). The Turonian to Albian is a key period for gold mineralization in the DVB.

6.4. Origin of gold deposits

LA–ICP–MS zircon U–Pb data (Fig. 6) of the rhyolitic ignimbrite from the Huangkeng Formation, the rhyolite from the Zhaixia Formation, the Xiaoshao syenogranite porphyry, and the post-mineralization granite porphyry dike bracket the duration of volcanism-subvolcanism in the Dongkeng district between 95.1 and 104 Ma (Cenomanian-Albian). The pyrite Re–Os age of 99 ± 10 Ma is shown to record the bulk Au mineralization in the DVB (Fig. 7). By inference, magmatism and gold mineralization in the DVB are comparable in time with the Cretaceous magmatism and metallogenesis in the SCFB at 110–80 Ma (Mao et al., 2008). During this period, the SCFB is considered to be under an extensional tectonic setting based on the wide distribution of the coeval A- and I-type composite granites (e.g., Li et al., 2014; Zhao et al., 2016), bimodal continental margin arc basalts and rhyolites (Xia et al., 2016), and pull-apart basins (Shu and Zhou, 2002). In this case, gold mineralization at Dongji and Maluntou is potentially occurred in the regional extensional setting. Apparently, this inference is strongly supported by the presence of comb quartz and cavities in the stgae 2 veins (Fig. A2).

Open-space filling, comb structures, various styles breccia mineralization at shallow levels, together with moderate-low temperature, low salinity fluids and low pressure (ca. 120 bar, discussed above), indicate an epithermal environment for ore system. In addition, the chemistry of pyrite is also used to constrain the origin of gold deposits. Generally, pyrite formed in epithermal stage is characterized by high As concentration (10^2-10^4 ppm) with Au concentration of 0.5-100 ppm (Sykora et al., 2018). The As and Au concentrations of pyrite2b range from 12 to 31528 ppm (average of 3457 ppm) and 0.11 to 27 ppm (average of 3.49 ppm) (Table A.2), and therefore well support the epithermal condition.

Cobalt and Ni contents, and Co/Ni ratios of pyrite are controlled by physical and chemical conditions of gold mineralization, and are considered to be empirical indicators to study the formation conditions (e.g., Li et al., 2015; Zhao et al., 2011). Co/Ni ratios for pyrite1, pyrite2b, and pyrite3 range 0.2−10.7 (mean = 4.3), 0.1−8.7 (mean = 2.2), and 0.4−4.9 (mean = 2.0) (Table A.2), are typical of magmatic-hydrothermal pyrite (Bajwah et al., 1987). The low Ni concentration (less than 98 ppm; Table 3) of pyrite from different generations also suggests a magmatic-hydrothermal origin, as pyrite from granite-related deposits is expected to contain negligible Ni (Rudnick and Gao, 2003). In this case, the formation of the Dongji and Maluntou gold deposits is potentially related to an epithermal magmatic-hydrothermal system. This suggestion is similar to the origin of most epithermal gold deposits in the SCFB (e.g., Zhong et al., 2017b; Chen et al., 2020).

The epithermal gold deposits in the SCFB are distinguished on the basis of the sulfidation state of the sulfide mineralogy, alteration zones, and geochemical associations as belonging to three sub-types: (1) high sulfidation (HS, e.g., Zijinshan, Li et al., 2017), (2) intermediate sulfidation (IS, e.g., Ancun, Li et al., 2018), and (3) low sulfidation types (LS, e.g., Yueyang and Shangshangang, Zhong et al., 2017b; Chen et al., 2020). The Dongji and Maluntou gold deposits potentially show many features in common with IS epithermal deposits (Heald et al., 1987; White and Hedenquist, 1995). For example, gold mineralization typically has a close temporal and spatial relationship with rhyolitic-dacitic volcanic-subvolcanic rocks (Chen et al., 2020), which is different from the LS ore system. In addition, the hydrothermal fluids generating gold deposits contain significant magma components and therefore with moderate-low temperatures (198−377 °C). Such temperatures are higher than the ones of typically LS deposits (e.g., Chen et al., 2020) but similar to some IS deposits (e.g., Wang et al., 2019). Einaudi et al. (2003) peoposed that the average Ag/Au concentration ratio in IS ore system should be more than 10. The ratio in this study is of 22 and thus supporting an IS epithermal origin. Moreover, hydrothermal alteration at Dongji and Maluntou is featured by assemblage of quartz-sericite-chlorite-illite, which is apparently different from kaolinite-adularia alteration in LS gold deposit in the DVB (Chen et al., 2020) and alunite-dickite alteration in HS gold deposit in the SCFB (Zhong et al., 2017).

Therefore, on the basis of our field and petrographic observations, LA–ICP–MS analysis results, pyrite Re–Os data, fluid inclusion studies, and characteristics of trace elements in pyrite, a possible scenario is proposed herein to explain the formation of IS epithermal gold deposits in the DVB. Volcanism-subvolcanism related to the regional extensional tectonic setting occurred during the 95–104 Ma and formed numerous pull-apart volcanic basins in the SCFB (e.g., the DVB). Hydrothermal fluids (H_2O−NaCl system) derived from the underlying magma chamber ascended along the volcanic vent to the epithermal environment and migrated to NE-trending faults at Dongji and NW-trending faults at Maluntou during ca. 99Ma.

The reaction between hydrothermal fluids and host rocks led to extensive hydrothermal alteration, e.g., sericitization and chloritization. However, the most important process was fluid boiling at ca. 329 °C with pressure of ca.120 bar, which potentially triggered the precipitation of massive ore-forming elements to form the sulfide quartz veins in the study area.

The Huaixi (Li et al., 2011), Jinjiyan (Zhong et al., 2017b), and Longtoushan (Wang, 2011) epithermal gold deposits within the SCFB (Fig. 1) possess similar characteristics with those exhibited by the Dongji and Maluntou deposits, and thus may also have an intermediate-sulfidation epithermal origin. The latter potentially proposes an entire metallogenic belt of intermediate-sulfidation epithermal deposits in the SCFB.

7. Conclusions

1. Hydrothermal fluids potentially had a magmatic component at high temperature (up to 377 °C; stage 1), and boiled at ca. 329 °C (stage 2), and mixed with infiltrating meteoric water during the late-stage (stage 3).
2. Visible gold and invisible gold are both closely associated with pyrite2b. Visible gold forms native gold and electrum and precipitates directly from the fluids during fluid boiling. Invisible gold is in the form of solid solution and related to lattice dislocations.
3. Gold mineralization in the Dongji deposit formed at ca. 99 Ma, which is coeval with volcanism-subvolcanism (95–104 Ma) related to the regional extensional tectonic setting.

4. Gold mineralization is related to an epithermal magmatic-hydrothermal system. The Dongji and Maluntou gold deposits have an intermediate-sulfidation epithermal origin.

Acknowledgements We express our thanks to reviewers for their critical reviews and comments. The authors also thank Editor-in-Chief Prof. Franco Pirajno and associated Editor-in-chief for their editorial help and constructive suggestions. Thanks are extended to Antonia Hofmann, Chris Ottley, Geoff Nowell, Zeyang Liu and Junjie Liu for analytical support of the Re–Os work, and Chenjin Chen from the Fujian goldmine for assistance during field work. This study was financially supported by the National Natural Science Foundation of China (grants No. 41772071), the Fundamental Research Fund of Xinjiang University (grant No. 620320026), and the Fund from the School of Earth Resource, China University of Geosciences (CUG, Wuhan) for Meng–Ting Chen during her study at Durham University, UK. DS acknowledges the Total Endowment Fund and the Dida Scholarship of CUG Wuhan.

Figure captions

Fig. 1 a Tectonic map of China showing the location of the Southeast China Fold Belt (SCFB). Revised after Zhong et al. (2017a). **b** Simplified geological map of the SCFB with Cretaceous volcanic basin, intrusions, and gold deposits. Modified after Chen et al., (2020). **c** Geology and distribution of gold deposits in the Dongkeng volcanic basin, showing the location of the Dongji and Maluntou deposits. Modified from Chen et al., (2020). NCC = North China Craton, YZC = Yangtze Craton, CB = Cathaysian Block, QHF = Qinzhou-Hangzhou Fault, ZDF =

Zhenghe-Dapu Fault, SYF = Shanghang-Yunxiao Fault, CSF = Chong'an-Shicheng Fault, CNF = Changle-Nan'ao Fault

Fig. 2 Geological maps of the Dongji (**a**) and Maluntou (**b**) gold deposits. Simplified and revised from Liu (2011) and Wang (2013). **c** Geological ichnography of the Dongji deposit at 416 elevations, showing the structurally controlled orebodies and post-mineralization granite porphyry, and locations for pyrite samples for Re–Os dating. **d** Typical hydrothermal alteration and zonation proximity to quartz-sulfide veins (the Maluntou deposit)

Fig. 3 Photos showing three mineralization stages and alteration characteristics of the Dongji gold deposit. **a-b** The stage 1 quartz veins are cut by the stage 2 sulfide-bearing quartz veins. **c-i** Ten pyrite separates collected from the stage 2 veins for Re–Os analyses. **j** The stage 2 quartz vein with chlorite and epidote halos is cut by stage 3 quartz vein. **k** The stage 3 barren quartz vein

Fig. 4 Photos showing three mineralization stages and alteration characteristics of the Maluntou gold deposit. **a** The stage 1 quartz vein with fine-grained pyrite (pyrite1) and K-feldspar halos. **b** Cross-cutting relationship between the stage 1 vein and stage 2 vein. **c** Mineral assemblage of the stage 2 quartz veins. **d** The stage 2 quartz vein with sulfide-bearing bands is cut by the stage 3 quartz vein

Fig. 5 Photomicrographs and scanning electron microscope (SEM) images illustrating the petrographic characteristics of sulfides in gold deposits. **a** Euhedral arsenopyrite is enveloped by pyrite1 in the stage 1 veins. **b** Pyrite2a is enveloped by pyrite2b within the stage 2 veins. **c** The relationship between pyrite2b and native gold. **d** Sulfide mineralogy of the stage 2 veins, including pyrite2b, chalcopyrite, galena, and sphalerite. **e** Coarse pyrite3 grains in the stage 3 veins. **f–h**. Unzoned texture of all types of pyrite

Fig. 6 Petrography, zircon CL images and LA–ICP–MS zircon U–Pb ages of early Cretaceous volcanic units at the DVB. **a** and **e** Rhyolitic ignimbrite (HK-1). **b** and **f** Rhyolite (ZX-1). **c** and **g** The xiaoshao syenogranite porphyry (XS-1). **d** and **h** The post-mineralization granite porphyry (DJ-1)

Fig. 7 a $^{187}Re/^{188}Os$ vs. $^{187}Os/^{188}Os$ plot for all data. **b** Plot of the percentage of deviation from the 139 Ma best-fit line. **c** Pyrite Re–Os best-fit lines based on initial $^{187}Os/^{188}Os$ data clusters and 99 Ma reference lines. See text for discussion. Data-point ellipses shown with 2s absolute uncertainty. MSWD = mean squared weighted deviation

Fig. 8 Distribution and characteristics of fluid inclusions in quartz veins. **a** Growth zone of quartz. **b** Distribution of primary and pseudosecondary fluid inclusions. **c** Linear distributed pseudosecondary fluid inclusions. **d** Liquid-rich two-phase FIA (type1). **e** Liquid-vapor two-phase FIA (type2). **f** Vapor-rich two-phase FIA (type3). **g**–**i** saline FIA (type4). j-l Laser Raman spectra for different fluid inclusion types.

Fig. 9 Homogenization temperature vs. Salinity, and histograms of homogenization temperatures of fluid inclusions from the different mineralization stages. Numbers with different colors indicate the FIA number discussed in the text. The fields of vein-type deposits, epithermal deposits, and porphyry deposits are modified from Wilkinson (2001)

Fig. 10 Representative time-resolved depth profiles showing distribution pattern of Fe, S, Co, Ni, Au, As, Cu, Zn, Ag, Sb, and Pb elements in four pyrite types. **a** Pyrite1. **b** Pyrite2a. **c** Pyrite2b. **d** Pyrite3

Fig. 11 Box and whisker plots of Co, Ni, Au, Cu, Ag, As, Pb, Zn, Sb and Ti contents in four pyrite types. The horizontal line represents the median, the solid black dot represents the mean, and the box represents the 25^{th} to 75^{th} percentile of the data. Whiskers are drawn to the last data point that is 2 times the length for the box from the maximum and minimum. Open circles are outliers

Fig. 12 Binary plots of As vs. Au (**a**). Co vs. Ni (**b**). Cu vs. Au (**c**). Ag vs. Sb (**d**). Pb vs. Sb (**e**). and Ag vs. Au (**f**) for different pyrite types. The trace element concentrations are from Table A.2, and all measurements below minimum detection limit are discarded. The Au-saturation line in (a) is defined by the equation $C_{Au} = 0.02 \times C_{As} + 4 \times 10^{-5}$, based on the study of Reich et al. (2005) that showed the maximum amount of Au that can be contained in the pyrite lattice is dependent on the As content

Fig. A.1 Summarized stratigraphic column for the Dongkeng volcanic basin

Fig. A.2 Plane polarized light (PPL) and cold-cathodoluminescence (CL) image of quartz formed in three mineralization stages (i.e., quartz1, 2, and 3). **a**–**b** Euhedral quartz crystals (quartz1) with bright brown fluorescence and growth zone are surrounded by anhedral quartz (quartz2) that shows blue fluorescence without growth zone. **c**–**f** The relationship between quartz2 and quartz3 (without any fluorescence)

References:

Bajwah ZU, Seccombe PK, Offler R (1987) Trace element distribution, Co: Ni ratios and genesis of the Big Cadia iron-copper deposit, New South Wales, Australia. Miner Deposita 22: 292–300

Baumgartner M, Bakker RJ, Doppler G (2014) Re-equilibration of natural H_2O–CO_2–salt-rich fluid inclusions in quartz—Part 1: experiments in pure water at constant pressures and differential pressures at 600° C. Contrib Mineral Petrol 168: 1017

Bodnar RJ (1993) Reviced equation and table for determining the freezing point depression of H_2O−NaCl solutions. Geochim Cosmochim Acta 57: 683–684

Canet C, Franco SI, Prol-Ledesma RM, González-Partida E, Villanueva-Estrada RE (2011) A model of boiling for fluid inclusion studies: Application to the Bolaños Ag–Au–Pb–Zn epithermal deposit, Western Mexico. J Geochem Explor 110: 118–125

Chang J, Li JW, Audétat A (2018) Formation and evolution of multistage magmatic-hydrothermal fluids at the Yulong porphyry Cu-Mo deposit, eastern Tibet: Insights from LA-ICP-MS analysis of fluid inclusions. Geochim Cosmochim Acta 232: 181–205

Chen MT, Wei JH, Li YJ, Shi WJ, Liu NZ (2020) Epithermal gold mineralization in Cretaceous volcanic belt, SE China: insight from the Shangshangang deposit. Ore Geol Rev 118: 103335

Chi GX, Haid T, Quirt D, Fayek M, Blamey N, Chu HX (2017) Petrography, fluid inclusion analysis, and geochronology of the End uranium deposit, Kiggavik, Nunavut, Canada. Miner Deposita 52: 211–232

Ciobanu CL, Cook NJ, Utsunomiya S, Kogagwa M, Green L, Gilbert S, Wade B (2012) Gold–telluride nanoparticles revealed in arsenic-free pyrite. Am Mineral 97: 1515–1518

Cook NJ, Chryssoulis SL (1990) Concentrations of invisible gold in the common sulfides. Can Mineral 28: 1–16

Cook NJ, Spry PG, Vokes FM (1998) Mineralogy and textural relationships among sulphosalts and related minerals in the Bleikvassli Zn-Pb-(Cu) deposit, Nordland, Norway. Miner Deposita 34: 35–56

Creaser RA, Papanastassiou DA, Wasserburg GJ (1991) Negative thermal ion mass spectrometry of osmium, rhenium and iridium. Geochim Cosmochim Acta 55: 397–401

Cumming VM, Selby D, Lillis PG, Lewan MD (2014) Re–Os geochronology and Os isotope fingerprinting of petroleum sourced from a Type I lacustrine kerogen: Insights from the natural Green River petroleum system in the Uinta Basin and hydrous pyrolysis experiments. Geochim Cosmochim Acta 138: 32–56

Deditius AP, Utsunomiya S, Renock D, Ewing RC, Ramana CV, Becker U, Kesler SE (2008) A proposed new type of arsenian pyrite: Composition, nanostructure and geological significance. Geochim Cosmochim Acta 72: 2919–2933

Driesner T, Heinrich CA (2007) The system H_2O–NaCl. Part I: Correlation formulae for phase relations in temperature–pressure–composition space from 0 to 1000 C, 0 to 5000 bar, and 0 to 1 XNaCl. Geochim Cosmochim Acta 71: 4880–4901

Einaudi MT, Hedenquist JW, Inan EE (2003) Sulfidation state of fluids in active and extinct hydrothermal systems: Transitions from porphyry to epithermal environments. Special Publication-Society of Economic Geologists 10: 285–314

Feng JW, Qiu ZL, Zhou WG, Chen D, Luo C, Chen WH (2016) The Geological Characteristics and Prospecting Marks of Gold Mineralization in Xiaoshao granite, South China. Mod Min: 119–122 (in Chinese with English abstract)

Guo F, Fan WM, Li CW, Zhao L, Li HX, Yang JH (2012) Multi-stage crust–mantle interaction in SE China: temporal, thermal and compositional constraints from the Mesozoic felsic volcanic rocks in eastern Guangdong–Fujian provinces. Lithos 150: 62–84

Hazarika P, Mishra B, Pruseth KL (2017) Trace-element geochemistry of pyrite and arsenopyrite: ore genetic implications for late Archean orogenic gold deposits in southern India. Mineral Mag 81: 661–678

Heald P, Foley NK, Hayba DO (1987) Comparative anatomy of volcanic-hosted epithermal deposits; acid-sulfate and adularia-sericite types. Econ Geol 82: 1–26

Hedenquist JW, Lowenstern JB (1994) The role of magmas in the formation of hydrothermal ore deposits. Nature 370: 519

Heinrich CA, Driesner T, Nsson AS, Seward TM (2004) Magmatic vapor contraction and the transport of gold from the porphyry environment to epithermal ore deposits. Geology 9: 761–764

Hu ZC, Zhang W, Liu YS, Gao S, Li M, Zong KQ, Chen HH, Hu SH (2014) “Wave” signal-smoothing and mercury-removing device for laser ablation quadrupole and multiple collector ICP–MS analysis: application to lead isotope analysis. Anal Chem 87: 1152–1157

Huston DL, Sie SH, Suter GF, Cooke DR, Both RA (1995) Trace elements in sulfide minerals from eastern Australian volcanic-hosted massive sulfide deposits; Part I, Proton microprobe analyses of pyrite, chalcopyrite, and sphalerite, and Part II, Selenium levels in pyrite; comparison with delta ^{34}S values and implications for the source of sulfur in volcanogenic hydrothermal systems. Econ Geol 90: 1167–1196

Jiang SH, Bagas L, Liang QL (2015) New insights into the petrogenesis of volcanic rocks in the Shanghang Basin in the Fujian Province, China. J Asian Earth Sci 105: 48–67

Jiang SH, Bagas L, Liang QL (2017) Pyrite Re–Os isotope systematics at the Zijinshan deposit of SW Fujian, China: Constraints on the timing and source of Cu-Au mineralization. Ore Geol Rev 80: 612–622

Li B, Jiang SY (2017) Genesis of the giant Zijinshan epithermal Cu-Au and Luoboling porphyry Cu–Mo deposits in the Zijinshan ore district, Fujian Province, SE China: A multi-isotope and trace element investigation. Ore Geol Rev 88: 753–767

Li SN, Ni P, Bao T, Xiang HL, Chi Z, Wang GG, Huang B, Ding JY, Dai BZ (2018) Genesis of the Ancun epithermal gold deposit, southeast China: Evidence from fluid inclusion and stable isotope data. J Geochem Explor 195:157–177

Li W, Cook NJ, Xie GQ, Mao JW, Ciobanu CL, Li JW, Zhang ZY (2019) Textures and trace element signatures of pyrite and arsenopyrite from the Gutaishan Au–Sb deposit, South China. Miner Deposita 54: 591–610

Li X (2000) Cretaceous magmatism and lithosphere extension in southeast China. J Asian Earth Sci 18: 293–305

Li YJ, Wei J, Tan J, Yao CL, Peng L, Xiao GL, Yan YF, Ye ZF (2011) Geochronologies of the Huaixi copper-gold deposit and the Caomen alkaline granite, SE China: implications for tectonic evolution. Int Geol Rev 53: 785–801

Li YJ, Wei JH, Tian N, Li H, Zhao SQ (2015) Geology, mineralogy, and geochemistry of fault-controlled hydrothermal Cu–Au mineralization in the Shanmen Volcanic Basin, SE China. Ore Geol Rev 64: 172–186

Li Z, Qiu JS, Yang XM (2014) A review of the geochronology and geochemistry of Late Yanshanian (Cretaceous) plutons along the Fujian coastal area of southeastern China: Implications for magma evolution related to slab break-off and rollback in the Cretaceous. Earth Sci Rev 128: 232–248

Liu AL, Jiang MR, Ulrich T, Zhang J, Zhang XJ (2018) Ore genesis of the Bake gold deposit, southeastern Guizhou province, China: Constraints from mineralogy, in-situ trace element and sulfur isotope analysis of pyrite. Ore Geol Rev 102: 740–756

Liu L, Xu XS, Zou HB (2012) Episodic eruptions of the Late Mesozoic volcanic sequences in southeastern Zhejiang, SE China: petrogenesis and implications for the geodynamics of paleo-Pacific subduction. Lithos 154: 166–180

Liu L, Xu XS, Xia Y (2016) Asynchronizing paleo-Pacific slab rollback beneath SE China: Insights from the episodic Late Mesozoic volcanism. Gondwana Res 37: 397–407

Liu NZ (2017) Analysis on the metallogenic physicochemical condition and the genesis of Maluntou gold deposit in the Zhenghe County, Fujian Province. Geol Fujian 36: 239–250 (in Chinese with English abstract)

Liu YF (2011) Geology and genesis of Dongji gold (silver) deposit in Fujian, South China. Geol Fujian 30: 21–28 (in Chinese with English abstract)

Liu YS, Hu ZC, Gao S, Günther D, Xu J, Gao CG, Chen HH (2008) In situ analysis of major and trace elements of anhydrous minerals by LA–ICP–MS without applying an internal standard. Chem Geol 257: 34–43

Lu Y, Zhou Y, Zhang HL, Yang K, Chen SZ, Xi WW, Xiu LC, Xing GF (2017) Hydrothermal alteration and its significance for exploration at the Dongji gold–silver deposit in Zhenghe, Fujian province. Geol Explor 53: 1039–1050 (in Chinese with English abstract)

Ludwig K (2008) Isoplot version 4.15: a geochronological toolkit for microsoft Excel. Berkeley Geochronology Center, Special Publication: 247–270

Mao JR, Zeng QT, Li ZL, Hu Q, Zhao XL, Ye HM (2008) Precise dating and geological significance of the Caledonian Shangyou pluton in South Jiangxi Province. Acta Geologica Sinica 82: 399–408

Mikucki EJ (1998) Hydrothermal transport and depositional processes in Archean lode-gold systems: A review. Ore Geol Rev 13: 307–321

Mumin AH, Fleet ME, Chryssoulis SL (1994) Gold mineralization in As-rich mesothermal gold ores of the Bogosu-Prestea mining district of the Ashanti Gold Belt, Ghana: remobilization of "invisible" gold. Miner Deposita 29: 445–460

Redmond PB, Einaudi MT, Inan EE, Landtwing MR, Heinrich CA (2004) Copper deposition by fluid cooling in intrusion-centered systems: New insights from the Bingham porphyry ore deposit, Utah. Geology 32: 217–220

Reich M, Kesler SE, Utsunomiya S, Palenik CS, Chryssoulis SL, Ewing RC (2005) Solubility of gold in arsenian pyrite. Geochim Cosmochim Acta 69: 2781–2796

Roedder E (1984) Fluid inclusions. Mineralogical Society of America, USA

Roedder E, Bodnar RJ (1980) Geologic pressure determinations from fluid inclusion studies. Annu Rev Earth Pl Sc 8: 263–301

Saintilan NJ, Selby D, Creaser RA, Dewaele S (2018) Sulphide Re–Os geochronology links orogenesis, salt and Cu–Co ores in the Central African Copperbelt. Sci Rep 8: 14946

Schaefer BF, Pearson DG, Rogers NW, Barnicoat AC (2010) Re–Os isotope and PGE constraints on the timing and origin of gold mineralisation in the Witwatersrand Basin. Chem Geol 276: 88–94

Selby D, Creaser RA (2001) Re-Os geochronology and systematics in molybdenite from the Endako porphyry molybdenum deposit, British Columbia, Canada. Econ Geol 96: 197–204

Selby D, Creaser RA, Fowler MG (2007) Re–Os elemental and isotopic systematics in crude oils. Geochim Cosmochim Acta 71: 378–386

Selby D, Kelley KD, Hitzman MW, Zieg J (2009) Re-Os sulfide (bornite, chalcopyrite, and pyrite) systematics of the carbonate-hosted copper deposits at Ruby Creek, southern Brooks Range, Alaska. Econ Geol 104: 437–444

Shu LS, Zhou XM (2002) Late Mesozoic tectonism of Southeast China. Geol Rev 48: 249–260 (in Chinese with English abstract)

Sibson RH, Robert F, Poulsen KH (1988) High-angle reverse faults, fluid-pressure cycling, and mesothermal gold-quartz deposits. Geology 16: 551–555

Stein HJ, Sundblad K, Markey RJ, Morgan JW, Motuza G (1998) Re–Os ages for Archean molybdenite and pyrite, Kuittila-Kivisuo, Finland and Proterozoic molybdenite, Kabeliai, Lithuania: Testing the chronometer in a metamorphic and metasomatic setting. Miner Deposita 33: 329–345

Stein HJ, Morgan JW, Scherstén A (2000) Re−Os dating of low-level highly radiogenic (LLHR) sulfides: The Harnas gold deposit, southwest Sweden, records continental-scale tectonic events. Econ Geol 95: 1657–167

Sung Y, Brugger J, Ciobanu CL, Pring A, Skinner W, Nugus M (2009) Invisible gold in arsenian pyrite and arsenopyrite from a multistage Archaean gold deposit: Sunrise Dam, Eastern Goldfields Province, Western Australia. Miner Deposita 44: 765–791

Sykora S, Cooke DR, Meffre S, Stephanov AS, Gardner K, Scott R, Selley D, Harris AC (2018) Evolution of pyrite trace element compositions from porphyry-style and epithermal conditions at the Lihir gold deposit: implications for ore genesis and mineral processing. Econ Geol 113: 193–208

Völkening J, Walczyk T, Heumann KG (1991) Osmium isotope ratio determinations by negative thermal ionization mass spectrometry. Int J Mass Spectrom 105: 147–159

Wang CH (2011) Metallogenic model and prognosis of the Longtoushan gold field, the Guangxi zhuang autonomous region. Doctor’s dissertation, China Chinese Academy of Geological Sciences, Beijing, pp 1–171 (in Chinese with English abstract)

Wang GG, Ni P, Zhao C, Chen H, Yuan HX, Cai YT, Li L, Zhu AD (2017) A combined fluid inclusion and isotopic geochemistry study of the Zhilingtou Mo deposit, South China: Implications for ore genesis and metallogenic setting. Ore Geol Rev 81: 884–897

Wang HB (2013) Metallogenic regularity and prospecting direction of gold deposits between Hudun of Zhenghe area and Dongyou of Jian'ou area, Fujian province. Master's thesis, China University of Geosciences, Beijing, pp 1–40 (in Chinese with English abstract)

Wang L,Qin KZ, Song GX, Li GM (2019) A review of intermediate sulfidation epithermal deposits and subclassification. Ore Geol Rev 107 434–456

White NC, Hedenquist JW (1995) Epithermal gold deposits: styles, characteristics and exploration. SEG newsletter 23: 9–13

Wilkinson JJ (2001) Fluid inclusions in hydrothermal ore deposits. Lithos 55: 229–272

Xia Y, Xu XS, Liu L (2016) Transition from adakitic to bimodal magmatism induced by the paleo-Pacific plate subduction and slab rollback beneath SE China: evidence from petrogenesis and tectonic setting of the dike swarms. Lithos 244: 182–204

Xiao F, Ban YZ (2015) S–Pb isotopes and typomorphic characteristics of pyrite in the Dongji gold (silver) deposit, Fujian province. Acta Mineralogica Sinica: 77–78 (in Chinese with English abstract)

Xu XB (2011) Research on Phanerozoic Structural Defonnation and Geochronology in Wuyishan area, South China. Doctor's dissertation, Nanjing University, Nanjing, pp 80–81 (in Chinese with English abstract)

Yang LQ, Deng J, Wang ZL, Guo LN, Li RH, Groves DI, Danyushevsky LV, Zhang C, Zheng XL, Zhao H (2016) Relationships between gold and pyrite at the Xincheng gold deposit, Jiaodong Peninsula, China: Implications for gold source and deposition in a brittle epizonal environment. Econ Geol 111: 105–126

Zeng QD, Wang YB, Zhang S, Liu JM, Qin KZ, Yang JH, Sun WD (2013) U–Pb and Re–Os geochronology of the Tongcun molybdenum deposit and Zhilingtou gold-silver deposit in Zhejiang Province, Southeast China, and its geological implications. Resour Geol 63: 99–109

Zhang X, Liu Q, Ma Y, Wang H (2005) Geology, fluid inclusions, isotope geochemistry, and geochronology of the Paishanlou shear zone-hosted gold deposit, North China Craton. Ore Geol Rev 26: 325–348

Zhao HX, Frimmel HE, Jiang SY, Dai BZ (2011) LA-ICP-MS trace element analysis of pyrite from the Xiaoqinling gold district, China: implications for ore genesis. Ore Geol Rev 43: 142–153

Zhao JL, Qiu JS, Liu L, Wang RQ (2016) The Late Cretaceous I-and A-type granite association of southeast China: Implications for the origin and evolution of post-collisional extensional magmatism. Lithos 240: 16–33

Zhong J, Pirajno F, Chen YJ (2017a) Epithermal deposits in South China: Geology, geochemistry, geochronology and tectonic setting. Gondwana Res 42: 193–219

Zhong J, Chen YJ, Qi JP, Chen J, Dai MC, Li J (2017b) Geology, fluid inclusion and stable isotope study of the Yueyang Ag–Au–Cu deposit, Zijinshan orefield, Fujian Province, China. Ore Geol Rev 86: 254–270

Zong KQ, Klemd R, Yuan Y, He ZY, Guo JL, Shi XL, Liu YS, Hu ZC, Zhang ZM (2017) The assembly of Rodinia: The correlation of early Neoproterozoic (ca. 900 Ma) high-grade metamorphism and continental arc formation in the southern Beishan Orogen, southern Central Asian Orogenic Belt (CAOB). Precambrian Res 290: 32–48

Zhou Z, Chen Y, Jiang S, Zhao H, Qin Y, Hu C (2014) Geology, geochemistry and ore genesis of the Wenyu gold deposit, Xiaoqinling gold field, Qinling Orogen, southern margin of North China Craton. Ore Geol Rev 59: 1-20

Figure 1

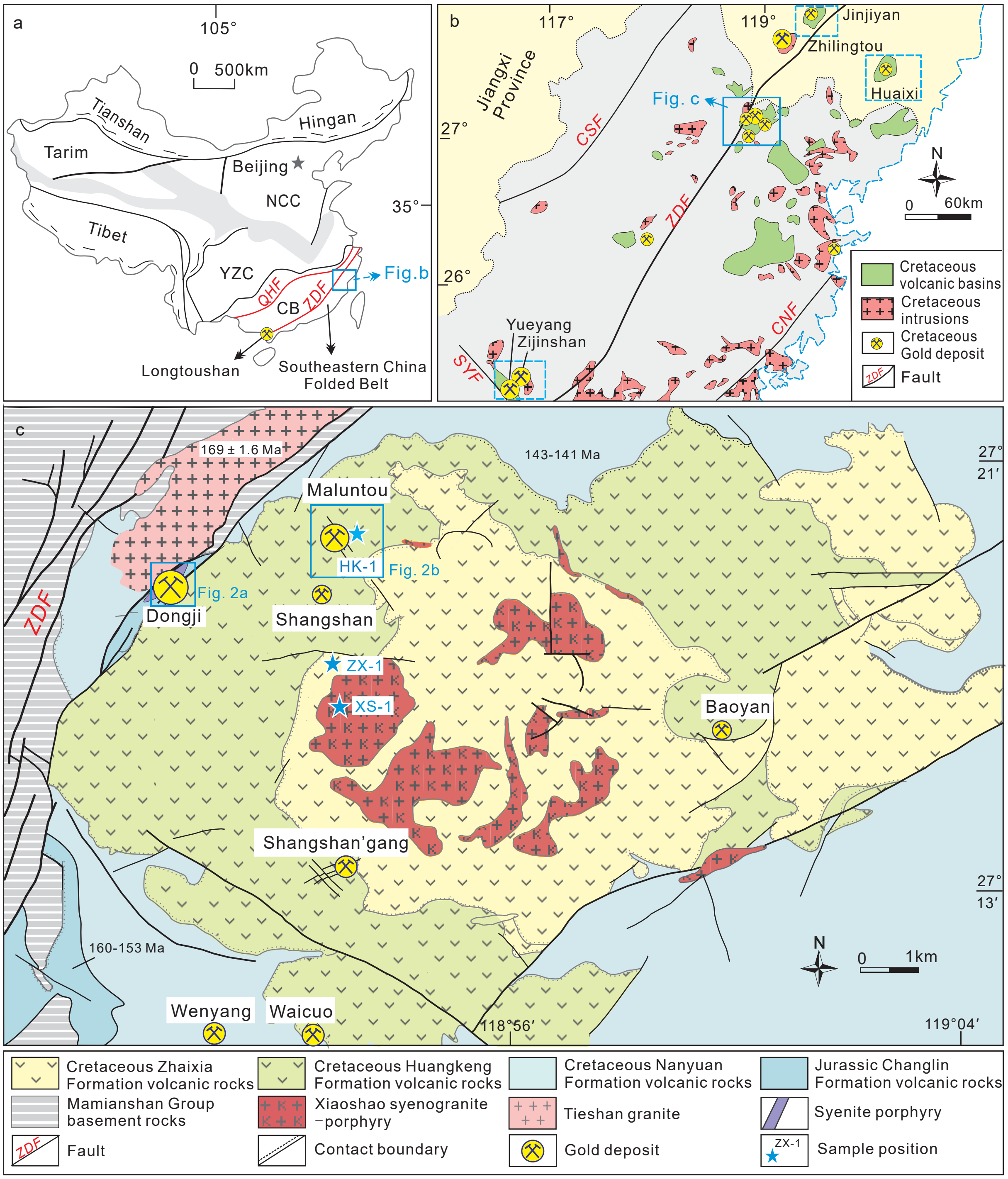
a
105°
0 500km
Tianshan
Hingan
Tarim
Beijing
NCC
35°
Tibet
YZC
QHF
CB
ZDF
Fig.b
Longtoushan
Southeastern China
Folded Belt
b
117°
119°
Jinjiyan
Zhilingtou
Huaixi
Jiangxi
Province
Fig. c
27°
CSF
ZDF
26°
N
0 60km
Cretaceous
volcanic basins
Cretaceous
intrusions
Cretaceous
Gold deposit
Fault
Yueyang
Zijinshan
SYF
CNF
c
169 ± 1.6 Ma
143-141 Ma
27°
21′
Maluntou
HK-1
Fig. 2b
Dongji
Fig. 2a
Shangshan
ZDF
ZX-1
XS-1
Baoyan
Shangshan’gang
27°
13′
N
0 1km
160-153 Ma
Wenyang
Waicuo
118°56′
119°04′
Cretaceous Zhaixia
Formation volcanic rocks
Cretaceous Huangkeng
Formation volcanic rocks
Cretaceous Nanyuan
Formation volcanic rocks
Jurassic Changlin
Formation volcanic rocks
Mamianshan Group
basement rocks
Xiaoshao syenogranite
−porphyry
Tieshan granite
Syenite porphyry
Fault
Contact boundary
Gold deposit
Sample position

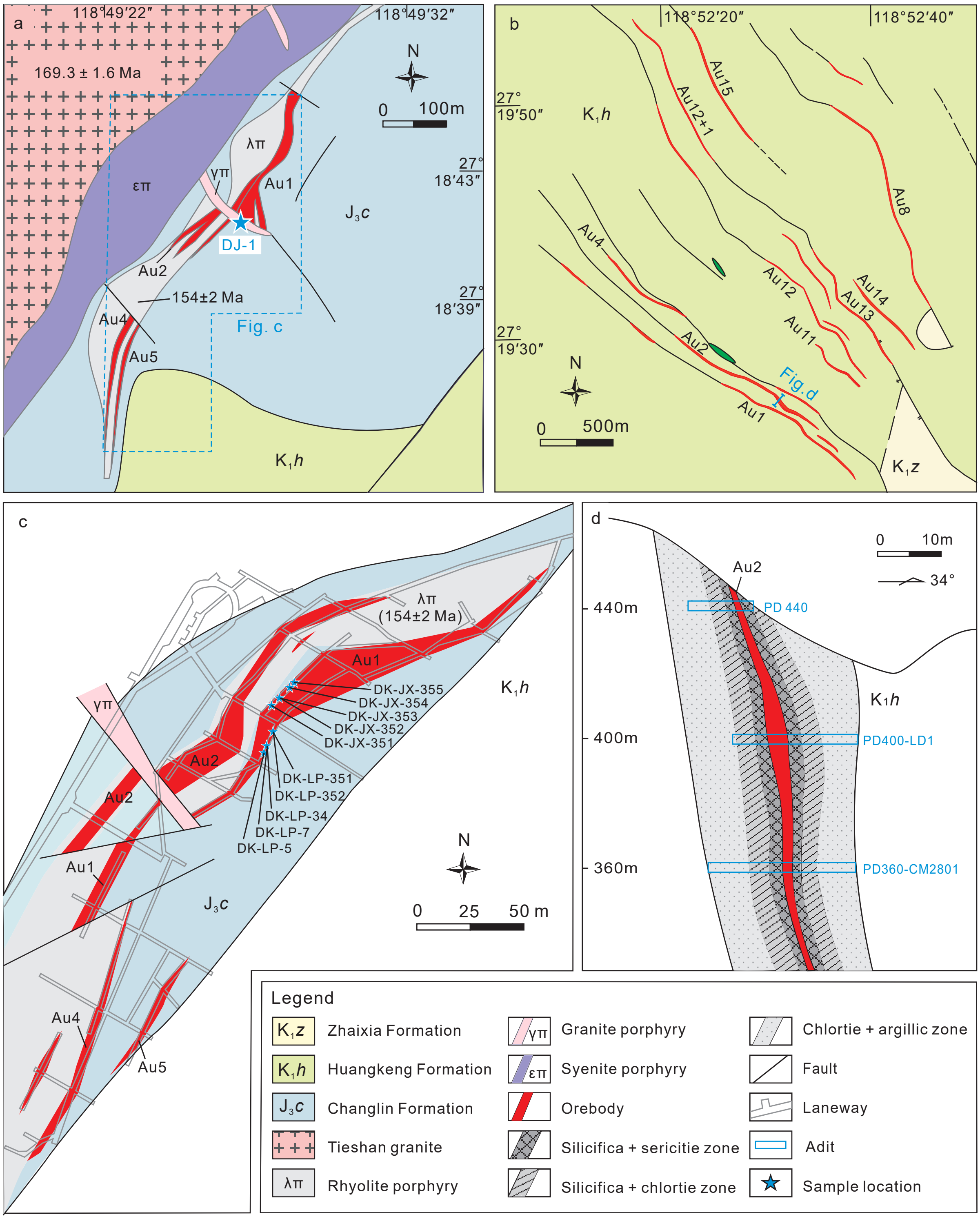
a
118°49′22″
118°49′32″
169.3 ± 1.6 Ma
N
0 100m
λπ
γπ
επ
Au1
27°
18′43″
J_3c
DJ-1
Au2
154±2 Ma
27°
18′39″
Au4
Fig. c
Au5
K_1h
b
118°52′20″
118°52′40″
27°
19′50″
K_1h
Au15
Au12+1
Au8
Au4
Au12
Au14
Au13
Au11
27°
19′30″
Au2
Fig.d
Au1
0 500m
K_1z
c
λπ
(154±2 Ma)
Au1
DK-JX-355
DK-JX-354
DK-JX-353
DK-JX-352
DK-JX-351
K_1h
γπ
Au2
Au2
DK-LP-351
DK-LP-352
DK-LP-34
DK-LP-7
DK-LP-5
Au1
J_3c
0 25 50 m
Au4
Au5
d
0 10m
Au2
34°
440m
PD 440
400m
PD400-LD1
K_1h
360m
PD360-CM2801
Legend
K_1z Zhaixia Formation
K_1h Huangkeng Formation
J_3c Changlin Formation
Tieshan granite
λπ Rhyolite porphyry
γπ Granite porphyry
επ Syenite porphyry
Orebody
Silicifica + sericitie zone
Silicifica + chlortie zone
Chlortie + argillic zone
Fault
Laneway
Adit
Sample location

Figure 3

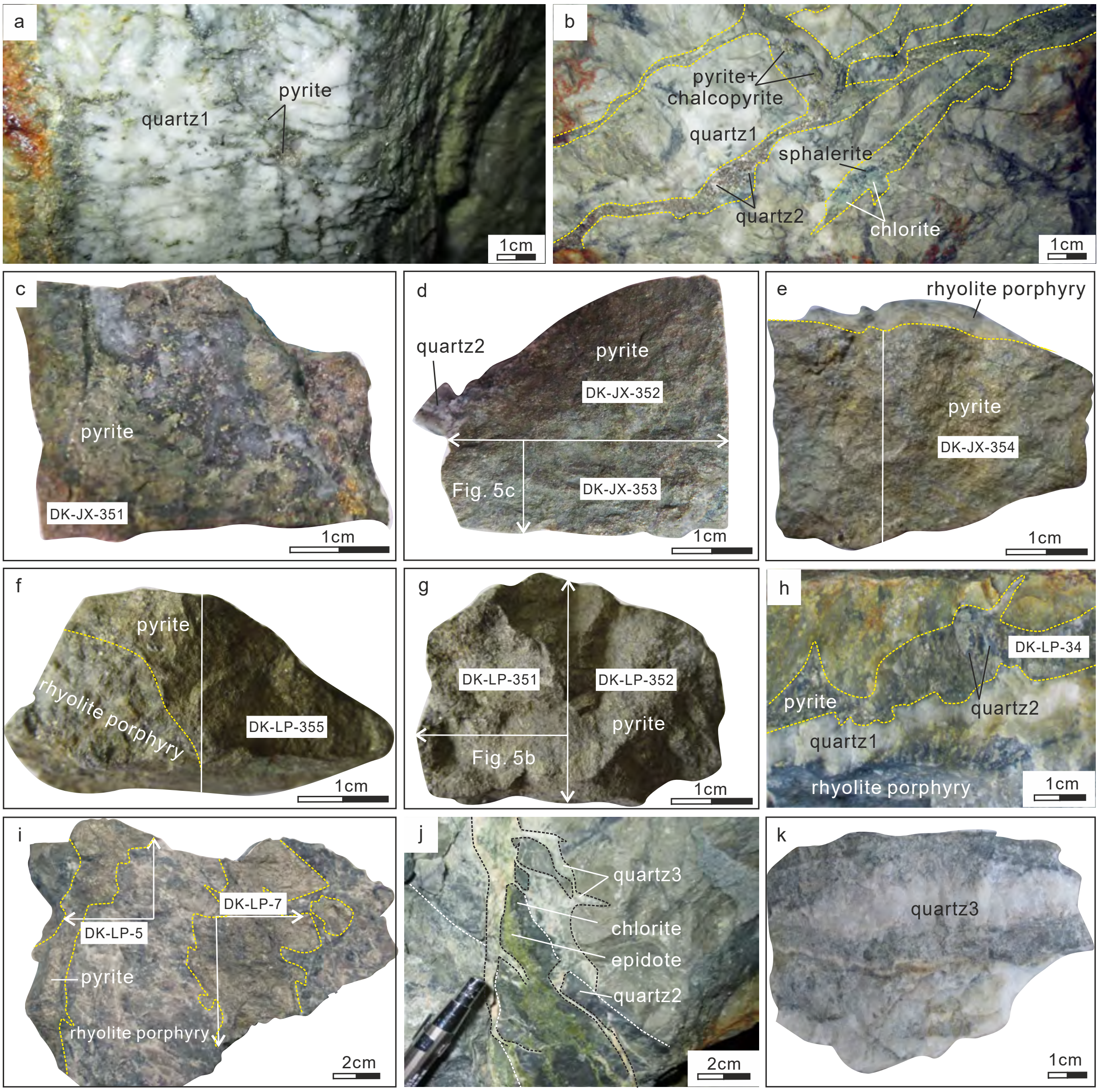
a
quartz1
pyrite
1cm
b
pyrite+
chalcopyrite
quartz1
sphalerite
quartz2
chlorite
1cm
c
pyrite
DK-JX-351
1cm
d
quartz2
pyrite
DK-JX-352
Fig. 5c
DK-JX-353
1cm
e
rhyolite porphyry
pyrite
DK-JX-354
1cm
f
pyrite
rhyolite porphyry
DK-LP-355
1cm
g
DK-LP-351
DK-LP-352
pyrite
Fig. 5b
1cm
h
DK-LP-34
pyrite
quartz2
quartz1
rhyolite porphyry
1cm
i
DK-LP-7
DK-LP-5
pyrite
rhyolite porphyry
2cm
j
quartz3
chlorite
epidote
quartz2
2cm
k
quartz3
1cm

Figure 4

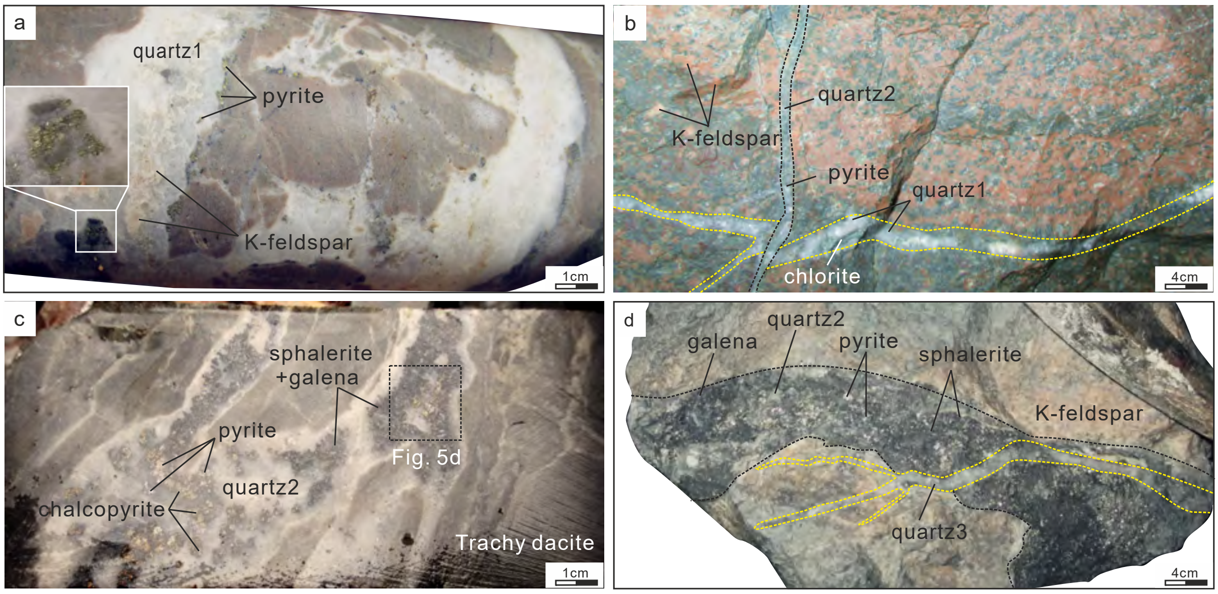
a
quartz1
pyrite
K-feldspar
1cm
b
quartz2
K-feldspar
pyrite
quartz1
chlorite
4cm
c
sphalerite
+galena
pyrite
quartz2
chalcopyrite
Fig. 5d
Trachy dacite
1cm
d
quartz2
galena
pyrite
sphalerite
K-feldspar
quartz3
4cm

Figure 5

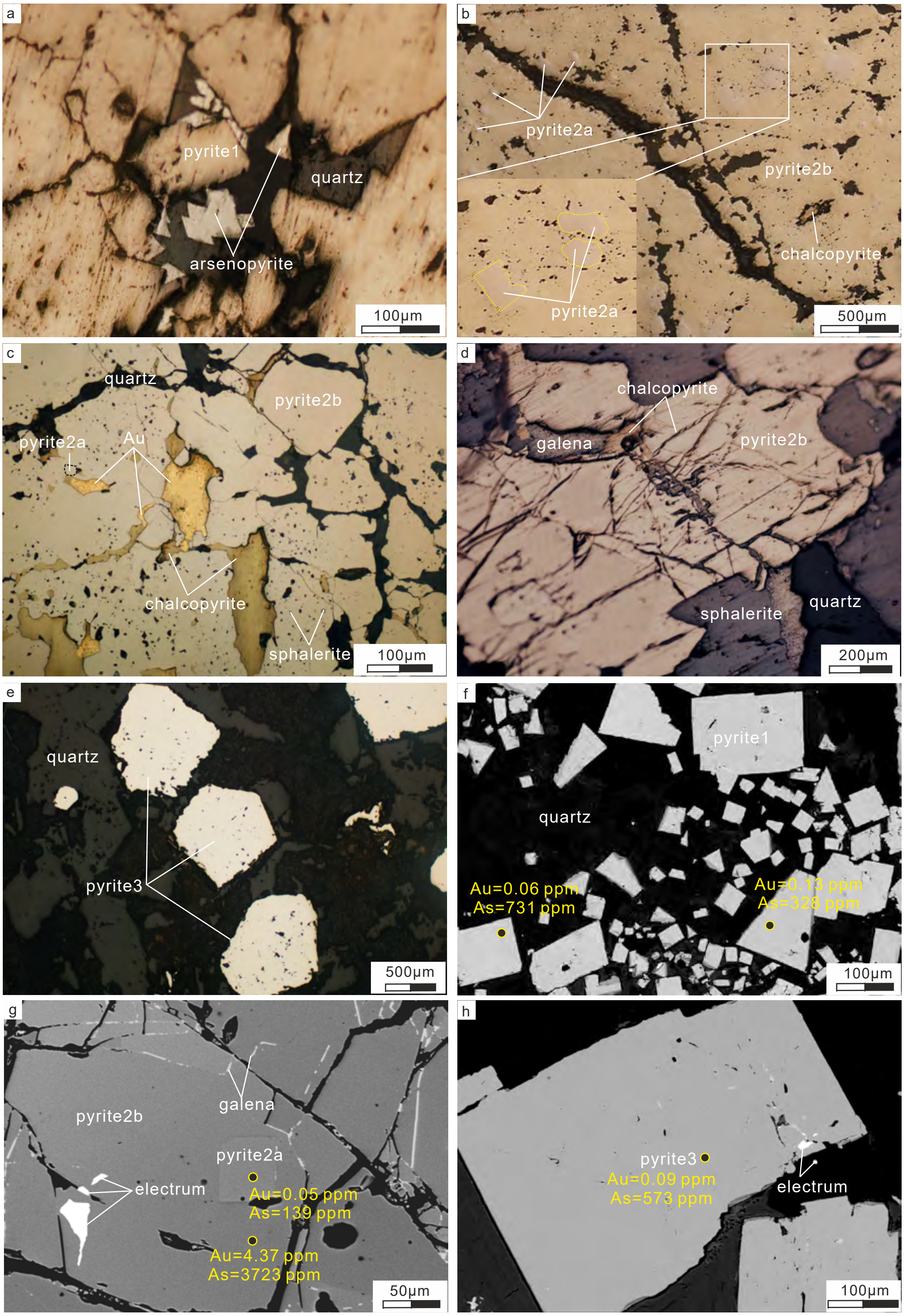
a
pyrite1
quartz
arsenopyrite
100μm
b
pyrite2a
pyrite2b
chalcopyrite
pyrite2a
500μm
c
quartz
pyrite2b
pyrite2a
Au
chalcopyrite
sphalerite
100μm
d
chalcopyrite
galena
pyrite2b
sphalerite
quartz
200μm
e
quartz
pyrite3
500μm
f
pyrite1
quartz
Au=0.06 ppm
As=731 ppm
Au=0.13 ppm
As=328 ppm
100μm
g
galena
pyrite2b
pyrite2a
electrum
Au=0.05 ppm
As=139 ppm
Au=4.37 ppm
As=3723 ppm
50μm
h
pyrite3
Au=0.09 ppm
As=573 ppm
electrum
100μm

Figure 6

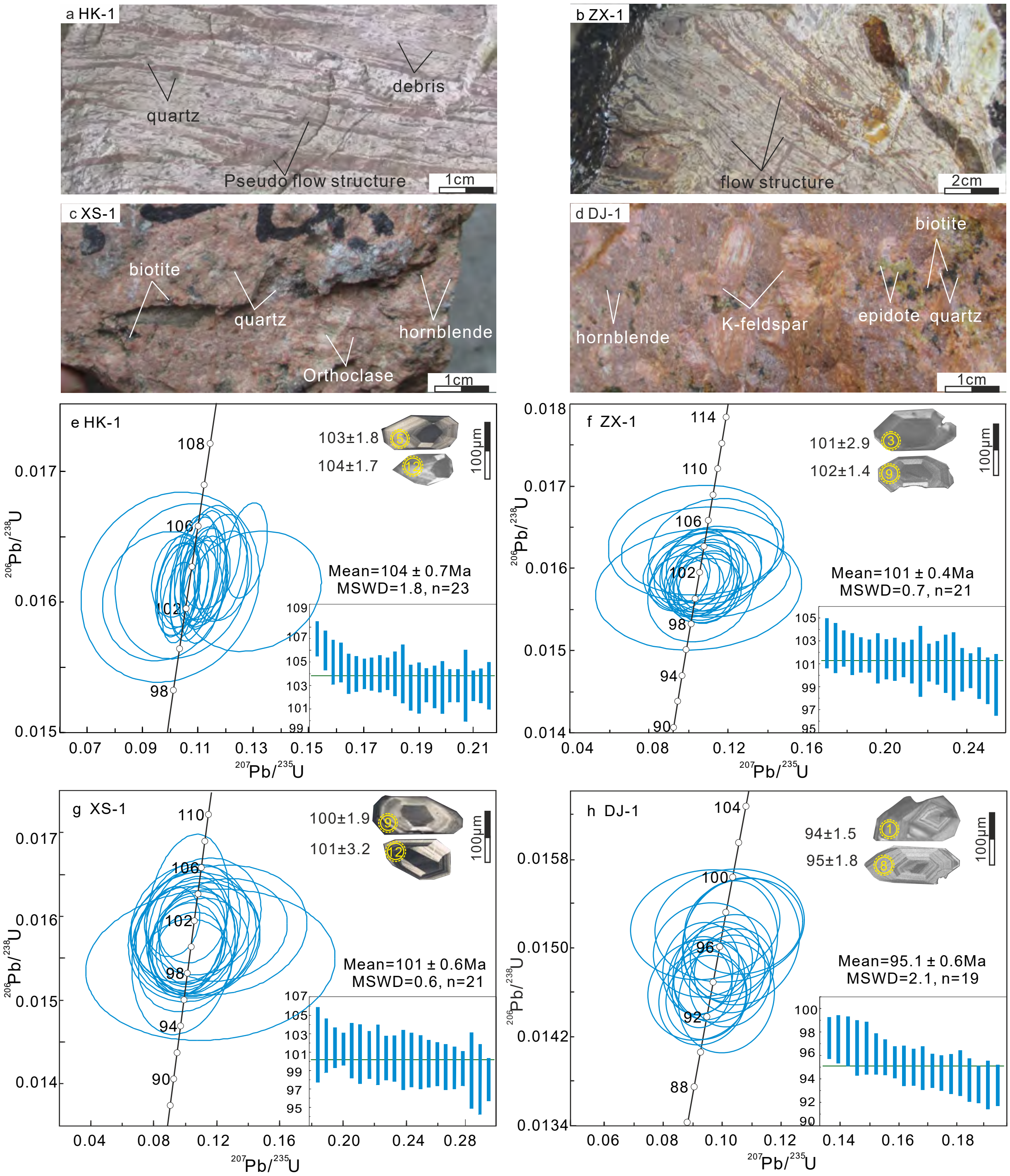
a HK-1
quartz
debris
Pseudo flow structure
1cm
b ZX-1
flow structure
2cm
c XS-1
biotite
quartz
hornblende
Orthoclase
1cm
d DJ-1
biotite
hornblende
K-feldspar
epidote
quartz
1cm
e HK-1
103±1.8
104±1.7
100μm
Mean=104 ± 0.7Ma
MSWD=1.8, n=23
f ZX-1
101±2.9
102±1.4
100μm
Mean=101 ± 0.4Ma
MSWD=0.7, n=21
g XS-1
100±1.9
101±3.2
100μm
Mean=101 ± 0.6Ma
MSWD=0.6, n=21
h DJ-1
94±1.5
95±1.8
100μm
Mean=95.1 ± 0.6Ma
MSWD=2.1, n=19
206Pb/238U
207Pb/235U

Figure 7

Click here to access/download;Figure;Fig. 7.pdf

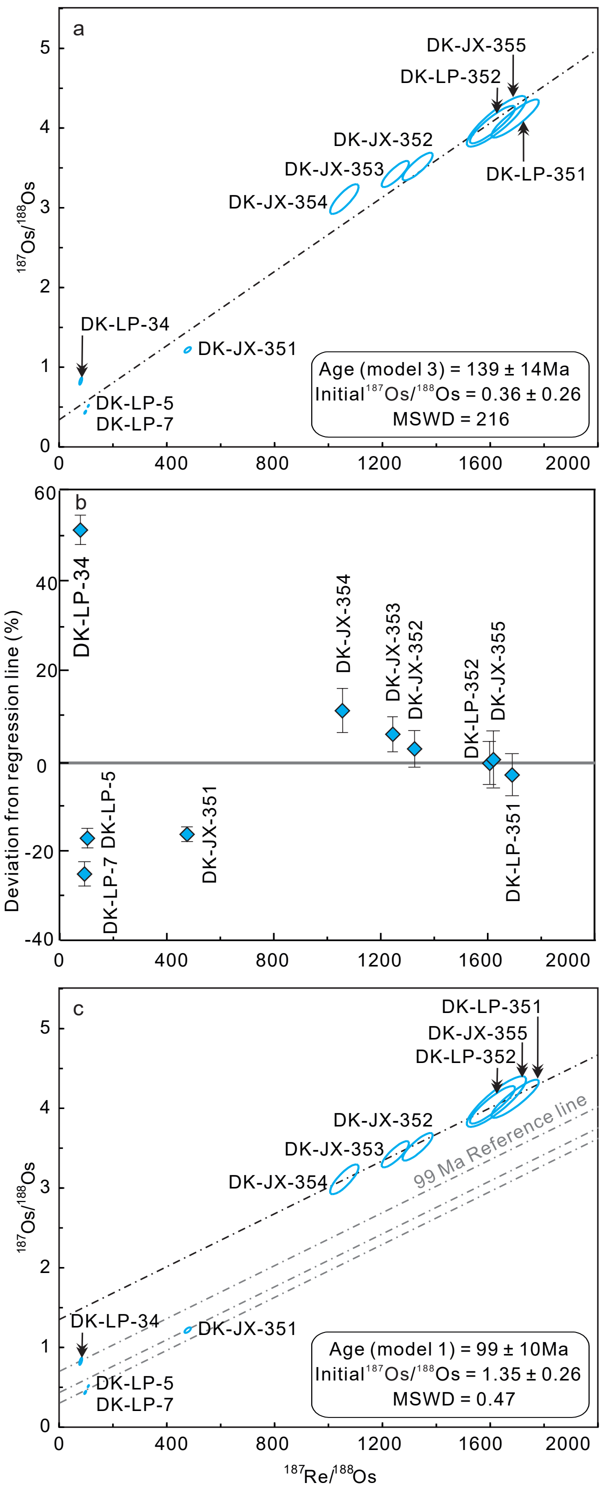

Figure 8

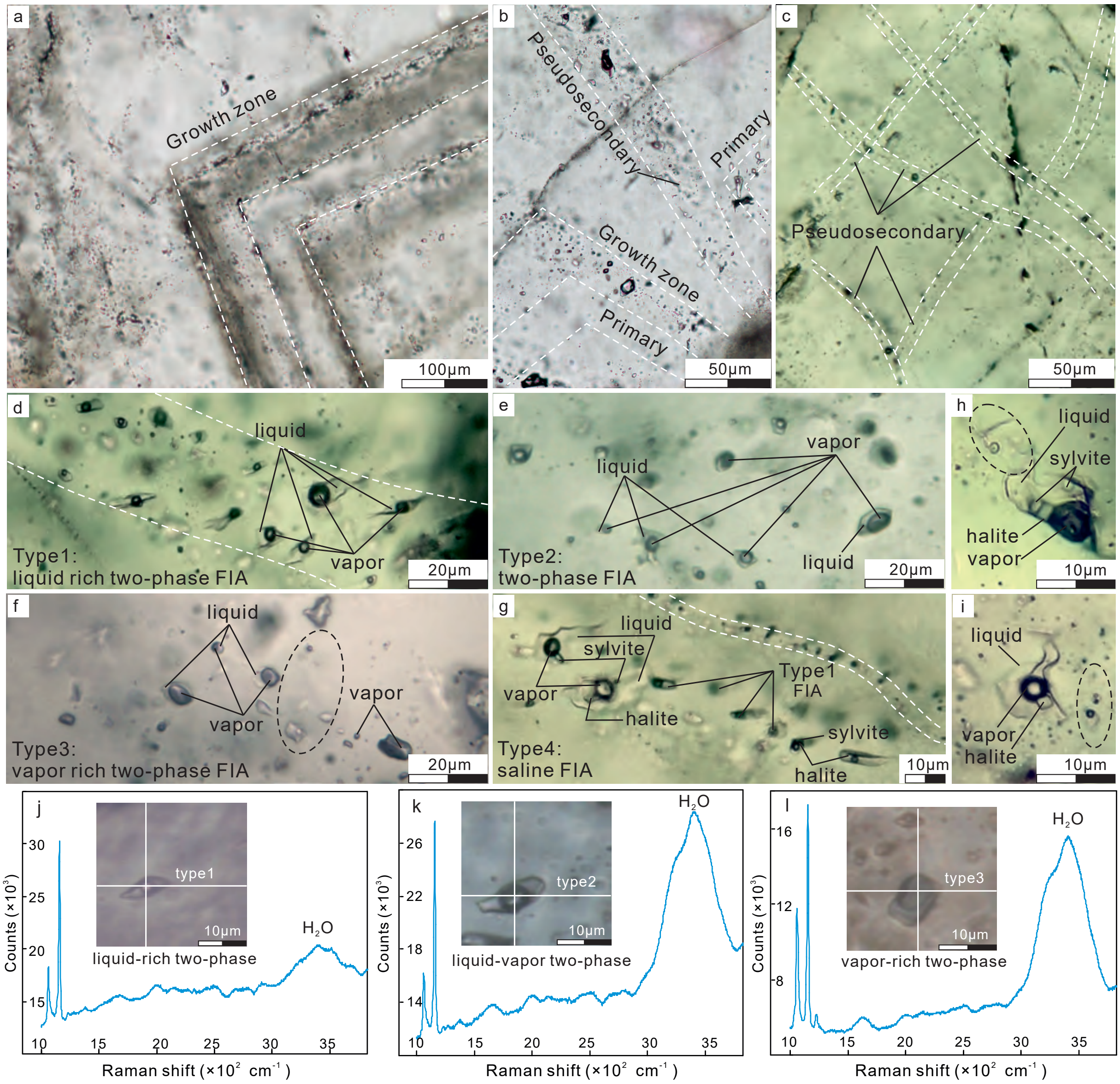
a
Growth zone
100μm
b
Pseudosecondary
Primary
Growth zone
Primary
50μm
c
Pseudosecondary
50μm
d
liquid
vapor
Type1:
liquid rich two-phase FIA
20μm
e
vapor
liquid
liquid
Type2:
two-phase FIA
20μm
h
liquid
sylvite
halite
vapor
10μm
f
liquid
vapor
vapor
Type3:
vapor rich two-phase FIA
20μm
g
liquid
sylvite
vapor
halite
Type1
FIA
sylvite
halite
Type4:
saline FIA
10μm
i
liquid
vapor
halite
10μm
j
Counts (×10³)
type1
10μm
liquid-rich two-phase
H₂O
Raman shift (×10² cm⁻¹)
k
Counts (×10³)
type2
10μm
liquid-vapor two-phase
H₂O
Raman shift (×10² cm⁻¹)
l
Counts (×10³)
type3
10μm
vapor-rich two-phase
H₂O
Raman shift (×10² cm⁻¹)

Figure 9

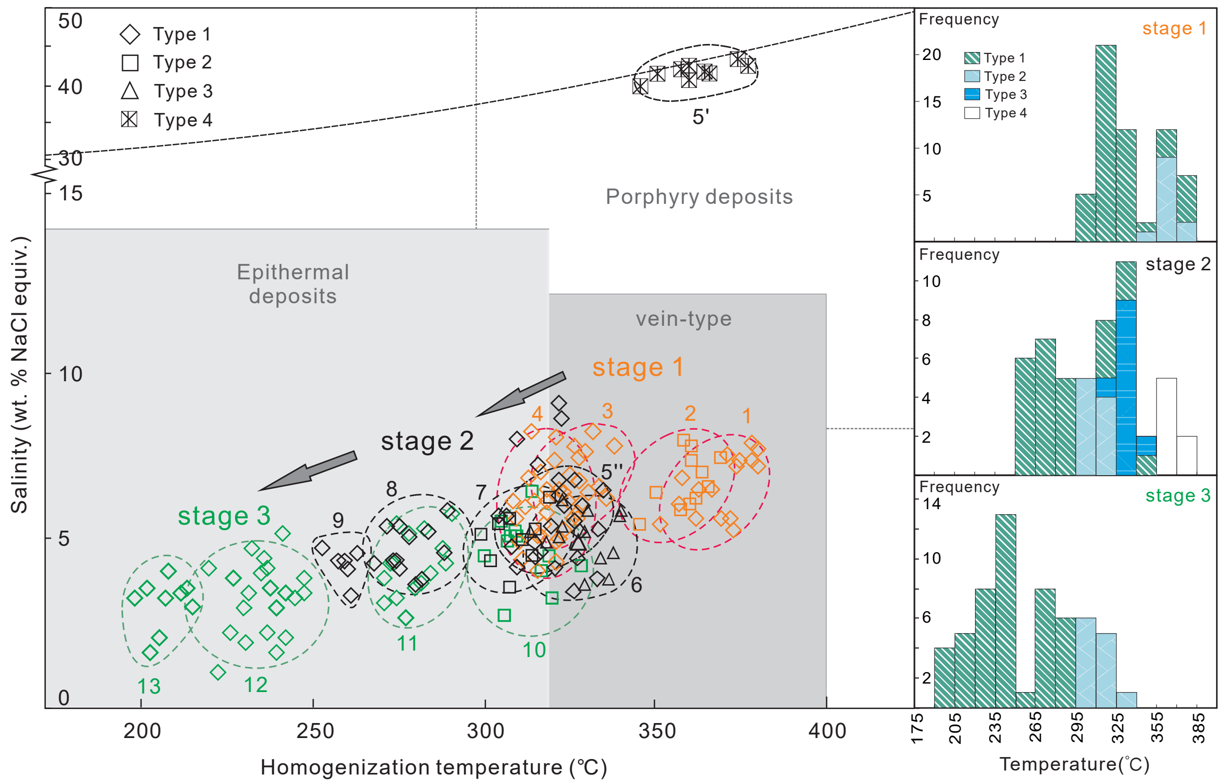

Type 1
Type 2
Type 3
Type 4
5'
Porphyry deposits
Epithermal
deposits
vein-type
stage 1
stage 2
stage 3
1
2
3
4
5''
6
7
8
9
10
11
12
13
Salinity (wt. % NaCl equiv.)
Homogenization temperature (℃)
0
5
10
15
30
40
50
200
250
300
350
400
Frequency
stage 1
stage 2
stage 3
Temperature(℃)
175
205
235
265
295
325
355
385

Figure 10

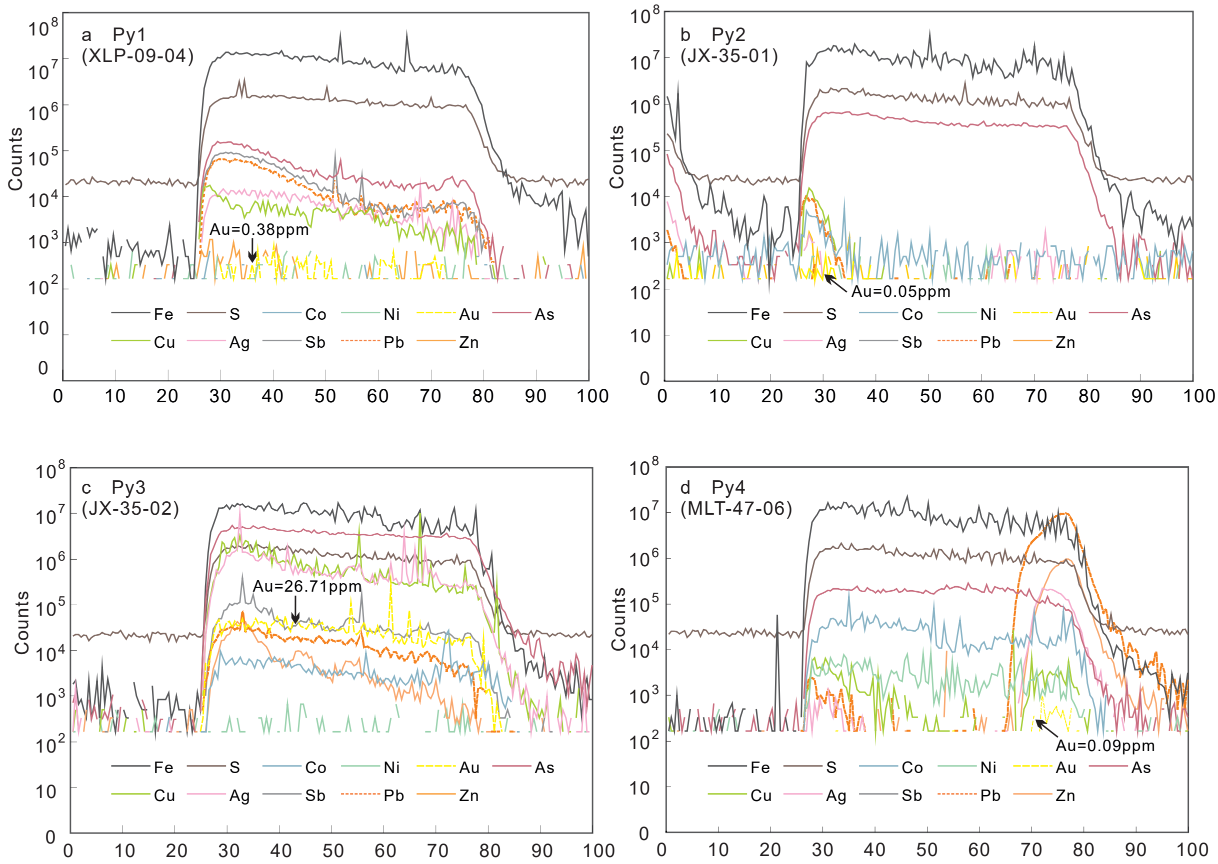
a Py1
(XLP-09-04)
Au=0.38ppm
b Py2
(JX-35-01)
Au=0.05ppm
c Py3
(JX-35-02)
Au=26.71ppm
d Py4
(MLT-47-06)
Au=0.09ppm
Counts
Fe S Co Ni Au As
Cu Ag Sb Pb Zn
0 10 20 30 40 50 60 70 80 90 100

Figure 11

Click here to access/download;Figure;Fig. 11.pdf

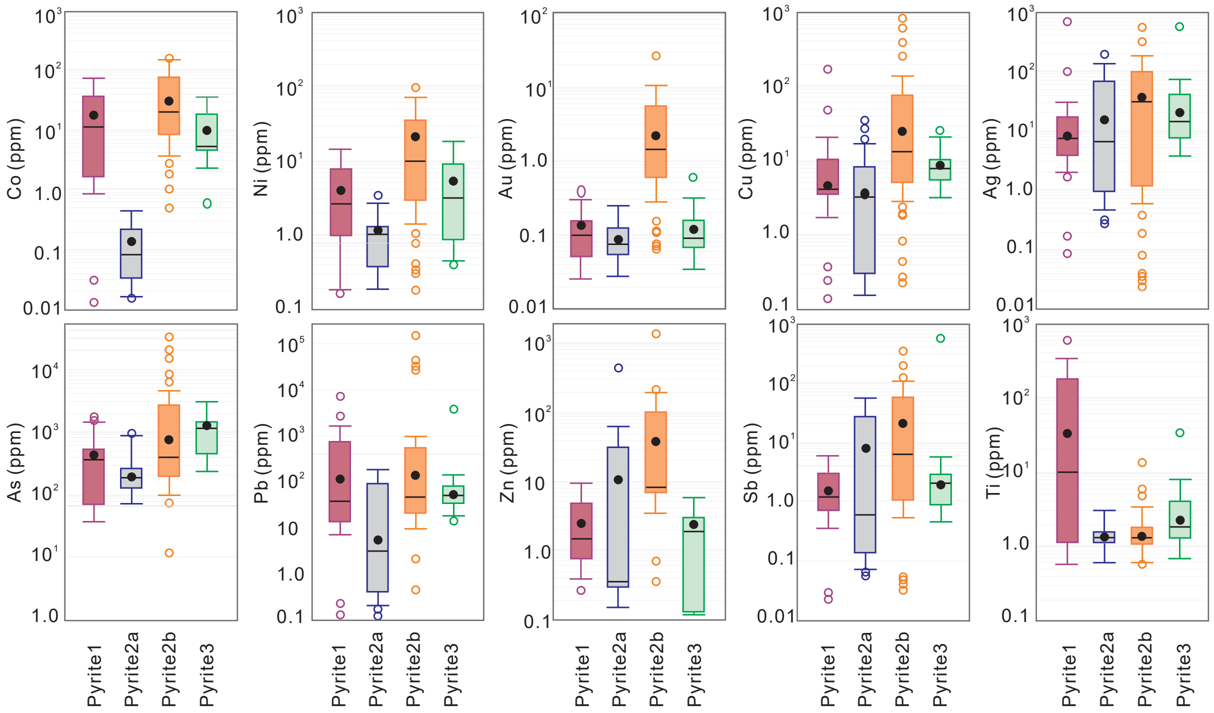

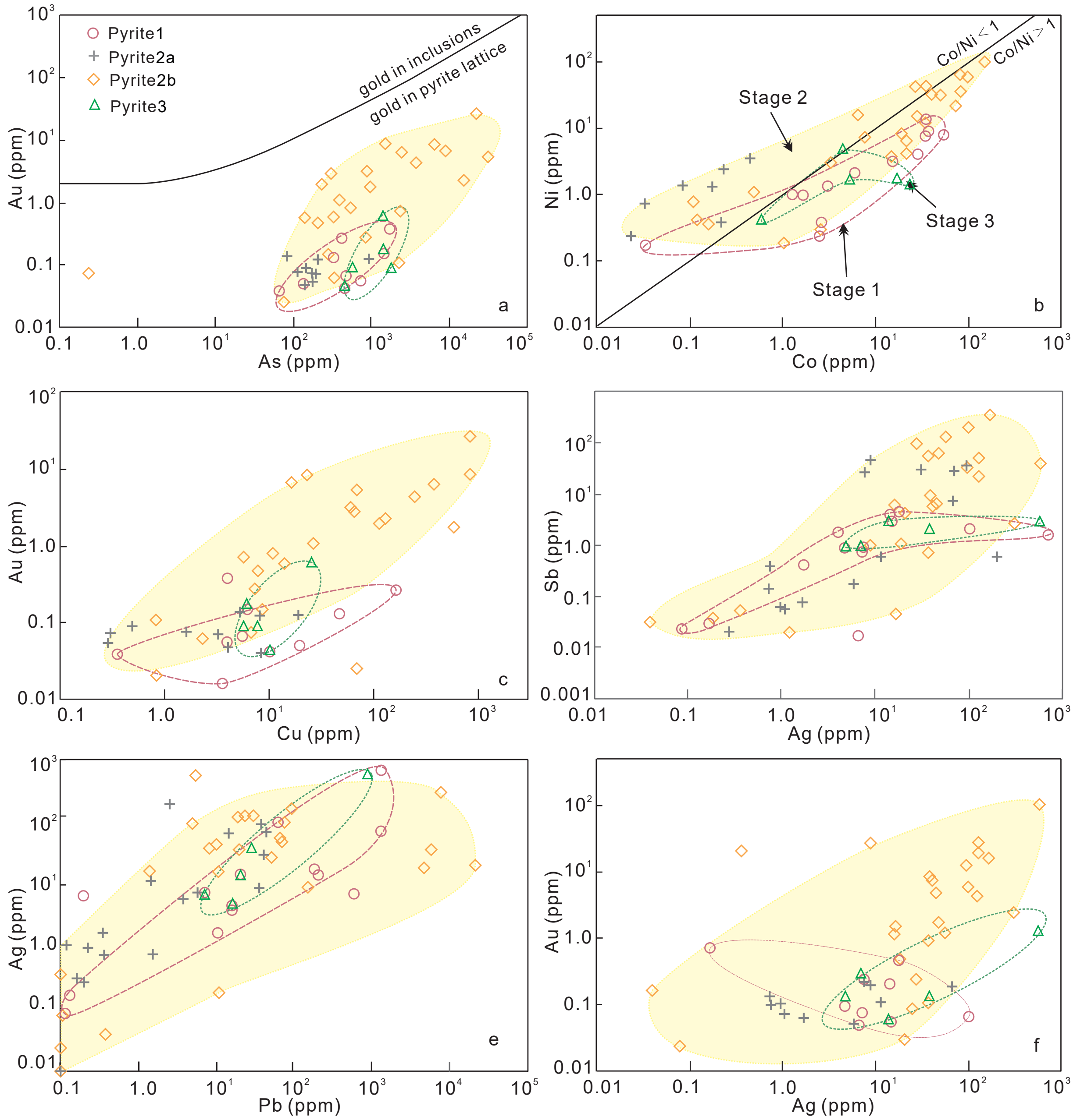
Pyrite1
Pyrite2a
Pyrite2b
Pyrite3
gold in inclusions
gold in pyrite lattice
Au (ppm)
As (ppm)
a
Stage 2
Stage 3
Stage 1
Co/Ni<1
Co/Ni>1
Ni (ppm)
Co (ppm)
b
Au (ppm)
Cu (ppm)
c
Sb (ppm)
Ag (ppm)
Ag (ppm)
Pb (ppm)
e
Au (ppm)
Ag (ppm)
f

Table 1

Re−Os isotopic data of pyrite2b dominated samples from the stage2 veins in the Dongji deposit.

Sample no	Location	Collected elevation	Ore type	Re (ppt-total)	±	Os (ppt-total)	±	%$^{187}Os^{r}$	$^{187}Re/^{188}Os$	±	$^{187}Os/^{188}Os$	±	Rho	Osi_{139}	Osi_{95}	Osi_{110}	Osi_{99}
DK-LP-35	Au1 orebody	416 m	Massive	996.0	3.6	4.3	0.1	66.7	1693.0	71.9	4.12	0.20	0.89	0.19	1.44	1.01	1.33
DK-LP-35	Au1 orebody	416 m	Massive	963.0	3.5	4.4	0.1	66.1	1608.5	68.3	4.04	0.19	0.89	0.31	1.50	1.09	1.39
DK-JX-35	Au1 orebody	416 m	Massive	1010.5	3.6	5.3	0.1	61.4	1331.0	46.0	3.52	0.14	0.85	0.43	1.41	1.08	1.32
DK-JX-35	Au1 orebody	416 m	Massive	1023.1	3.7	5.6	0.1	60.4	1248.1	41.4	3.42	0.13	0.84	0.53	1.45	1.13	1.36
DK-JX-35	Au1 orebody	416 m	Massive	802.9	2.9	5.1	0.1	56.0	1058.8	43.4	3.11	0.15	0.82	0.65	1.43	1.17	1.36
DK-JX-35	Au1 orebody	416 m	Massive	916.5	3.3	4.1	0.1	65.4	1623.5	90.2	4.09	0.26	0.87	0.32	1.51	1.11	1.41
DK-LP-5	Au1 orebody	416 m	Massive	874.3	3.2	40.8	0.2	35.0	108.4	1.1	0.51	0.01	0.62	0.26	0.34	0.31	0.33
DK-LP-7	Au1 orebody	416 m	Massive	115.0	1.0	5.9	0.0	23.6	96.8	2.1	0.43	0.01	0.68	0.21	0.28	0.26	0.27
DK-JX-35	Au1 orebody	416 m	Massive	1111.4	5.0	12.8	0.1	72.7	477.8	6.5	1.22	0.02	0.74	0.11	0.46	0.34	0.43
DK-LP-34	Au1 orebody	416 m	Disseminated	62.8	0.9	4.1	0.0	21.0	80.9	2.6	0.83	0.03	0.75	0.64	0.70	0.68	0.69

Abbreviations: %$^{187}Os^{r}$ = the percentage of radiogenic ^{187}Os in ^{187}Os budget; Osi_{139} = initial $^{187}Os/^{188}Os$ ratio at 139 Ma; Osi_{95} = initial $^{187}Os/^{188}Os$ ratio at 95 Ma; Osi_{110} = initial $^{187}Os/^{188}Os$ ratio at 110 Ma; Rho = error correlation of the $^{187}Re/^{188}Os$ and $^{187}Os/^{188}Os$.

Table 2

Microthermometric data of different fluid inclusion assemblages in quartz veins from three mineralization stages at the Dongkeng volcanic basin.

Stage	FIAs No.	Sample details			Mineral	Characteristics	Classification	Mode	Microthermometry (°C)		
		Sample No.	Elevation (m)	Lode					*T* m,H	*T* m,ice	*T* h,total (n)
Stage 1	1	DJ-40-1	145	Au1	Quartz1	Liquid-rich two-phase fluid inclusions	Type 1	L		-6.0 to -3.5	353−377 (20)
	2	DJ-40-2	145	Au1	Quartz1	Liquid-vapor two-phase fluid inclusions	Type 2	L		-5.2 to -3.6	347−369 (12)
	3	MLT-19	360	Au17	Quartz1	Liquid-rich two-phase fluid inclusions	Type 1	L		-5.1 to -2.9	320−342 (15)
	4	DJ-32	100	Au1	Quartz1	Liquid-rich two-phase fluid inclusions	Type 1	L		-5.1 to -2.8	308−328 (24)
Stage 2	5	DJ-35-1	145	Au1	Quartz2	Liquid-rich two-phase fluid inclusions and Halite-bearing fluid inclusions	Type 1	L		-5.6 to -2.7	306−335 (13)
							Type 4	L	327−359		345−374 (9)
	6	DJ-35-2	145	Au1	Quartz2	Liquid-rich two-phase fluid inclusions and Vapor-rich two-phase fluid inclusions	Type 1	L		-3.3 to -2.1	328−341 (11)
							Type 3	V		-3.8 to -2.1	318-340 (15)
	7	DJ-13	100	Au1	Quartz2	Liquid-vapor two-phase fluid inclusions	Type 2	L		-3.9 to -2.1	298−320 (9)
	8	MLT-2	300	Au17	Quartz2	liquid-rich two-phase fluid inclusions	Type 1	L		-3.6 to -2.1	268−290 (12)
	9	MLT-17	360	Au17	Quartz2	liquid-rich two-phase fluid inclusions	Type 1	L		-2.9 to -1.9	253−269 (6)
Stage 3	10	DJ-29	145	Au1	Quartz3	Liquid-vapor two-phase fluid inclusions	Type 2	L		-4.0 to -1.6	300−329 (12)
	11	DJ-40	200	Au1	Quartz3	liquid-rich two-phase fluid inclusions	Type 1	L		-3.5 to -1.5	271−300 (15)
	12	MLT-9	300	Au17	Quartz3	liquid-rich two-phase fluid inclusions	Type 1	L		-2.8 to -0.6	223−249 (21)
	13	MLT-16	260	Au17	Quartz3	liquid-rich two-phase fluid inclusions	Type 1	L		-2.4 to -0.9	198−215 (9)

All temperatures in °C. Salinity expressed as wt% NaCl equivalent. Mode, fluid inclusion totally homogenized to liquid (L) or vapor (V) phase; Tm,H, melting temperature c
Tm,ice, temperature of final ice melting; Th,total, temperature of total homogenization; n, number of individual fluid inclusions measured within a sample.

Salinity (wt% NaCl equiv.)
5.7−9.1
5.8−8.2
4.8−8.4
4.6−8.4
4.1−9.1
40.4−42.4
3.6−5.4
3.5−6.2
3.5−6.3
3.5−5.9
3.2−4.8
2.7−6.5
2.5−5.7
1.0−5.1
1.5−4.1

[f] halite dissolution;

Table 3

Table 3

Summary of LA−ICP−MS data on elemental concentrations in four pyrite types (in ppm).

	No. analysis	As	Au	Ag	Pb	Zn	Cu	Ti	Co	Ni	Mo	Sb	Bi	Tl
Pyrite1	14													
Geometric Mean Values		478	0.13	69	748	1.9	20	91	17	3.9	7.4	1.5	0.49	0.09
Median Values		375	0.10	7.4	37	1.5	4.0	10	11	2.6	2.3	1.2	0.31	0.09
Max Values		1710	0.38	713	6305	5.3	165	606	54	14	26	4.6	2.0	0.18
Min Values		bdl	bdl	bdl	bdl	bdl	0.14	0.61	bdl	bdl	bdl	bdl	bdl	bdl
Pyrite2a	18													
Geometric Mean Values		306	0.08	32	30	48	7.7	1.3	0.14	1.3	0.79	12	0.03	6.5
Median Values		192	0.07	6.8	3.3	0.21	3.3	1.3	0.08	1.0	0.34	0.60	0.01	0.06
Max Values		952	0.14	203	119	451	35	1.9	0.44	3.5	3.4	46	0.07	51.9
Min Values		bdl	bdl	bdl	bdl	bdl	bdl	0.98	bdl	bdl	bdl	bdl	bdl	bdl
Pyrite2b														
Geometric Mean Val	31	3457	3.5	78	11520	101	116	2.1	31	21	65	43	0.56	2.8
Median Values		404	1.4	38	52	8.1	14	1.3	20	10	0.06	6.4	0.24	0.09
Max Values		31528	27	589	######	1419	852	14	150	98	1217	341	3.8	55.9
Min Values		bdl	bdl	bdl	bdl	bdl	bdl	0.57	bdl	bdl	bdl	bdl	bdl	bdl
Pyrite3	5													
Geometric Mean Values		1134	0.20	128	829	2.3	11	9.0	10	6.3	7.9	1.9	0.48	0.08
Median Values		1403	0.09	14	50	1.9	7.8	3.8	5.2	3.2	2.0	2.1	0.27	0.07
Max Values		1807	0.60	574	3967	4.7	26	34	23	16	19	2.8	1.2	0.20
Min Values		455	0.04	4.8	15	bdl	5.8	1.3	0.59	0.90	0.01	0.90	0.01	0.02
Average minimum detection limit		0.277	0.036	0.051	0.124	0.246	0.071	0.186	0.017	####	####	####	####	0.013

The values of “bdl” mean the contents are below minimum detection limits

Click here to access/download
Supplementary Material
Table A.1.xls